

Drug-Target Graph based Recurrent Network for Drug Combination Prediction

Yuqi Wen

Institute of Health Service and Transfusion Medicine

Zhiwei Cao

School of Informatics, Xiamen University

Yixin Zhang

Institute of Health Service and Transfusion Medicine

Lianlian Wu

Tianjin University <https://orcid.org/0000-0002-9611-4488>

Zhongming Wang

Academy of Medical Engineering and Translational Medicine, Tianjin University

Chong Dai

College of Life Science and Technology, Beijing University of Chemical Technology

Jing Wang

School of Medicine, Tsinghua University

Dongjin Leng

Institute of Health Service and Transfusion Medicine

Jinsong Su

School of Informatics, Xiamen University

Song He

Institute of Health Service and Transfusion Medicine <https://orcid.org/0000-0002-4136-6151>

Xiaochen Bo (✉ boxiaoc@163.com)

Institute of Health Service and Transfusion Medicine <https://orcid.org/0000-0003-3490-5812>

Article

Keywords:

Posted Date: March 23rd, 2022

DOI: <https://doi.org/10.21203/rs.3.rs-1406217/v1>

License:   This work is licensed under a Creative Commons Attribution 4.0 International License.

[Read Full License](#)

1 Drug-Target Graph based Recurrent Network for 2 Drug Combination Prediction

3 Yuqi Wen^{1,6}, Zhiwei Cao^{2,6}, Yixin Zhang^{1,6}, Lianlian Wu^{3,1,6}, Zhongming Wang^{3,1},
4 Chong Dai^{4,1}, Jing Wang^{5,1}, Dongjin Leng¹, Jinsong Su^{2,7,*}, Song He^{1,7,*} & Xiaochen
5 Bo^{1,3,7,*}

6 Abstract

7 Compared with monotherapy, drug combination therapy has demonstrated more effective and
8 powerful therapeutic effects in cancer treatment. However, due to the large size of the
9 combinatorial space, experimental identification of synergistic drug combinations is cost- and
10 time-consuming, even with high-throughput screens. With the accumulation of various types of
11 drug informatics data, artificial intelligence techniques have become applicable for the prediction
12 of synergistic drug combinations, thereby reducing the experimental workload and accelerating
13 the discovery of combination therapy. Currently, the emerging graph neural network (GNN) has
14 been applied to drug combination prediction and brings new insight on the discovery of
15 combination therapy. In this study, we proposed Drug-Target Graph based Recurrent Network
16 (DTGRN) to predict synergistic drug combinations in various cancer cell lines. Specifically, we
17 proposed a Graph Recurrent Network-based encoder to learn a low-dimensional representation of
18 features for each node and then predicted the synergy score of novel drug combinations based on
19 these representations via a cell line-specific projection matrix. In DTGRN, gating mechanism and
20 cell-line-level states are employed to ensure each node representation more comprehensively

¹Institute of Health Service and Transfusion Medicine, Beijing, China. ²School of Informatics, Xiamen University, Xiamen, China. ³Academy of Medical Engineering and Translational Medicine, Tianjin University, Tianjin, China. ⁴College of Life Science and Technology, Beijing University of Chemical Technology, Beijing, China. ⁵School of Medicine, Tsinghua University, Beijing, China. ⁶These authors contributed equally: Yuqi Wen, Zhiwei Cao, Yixin Zhang, Lianlian Wu. ⁷These authors jointly supervised this work: Xiaochen Bo, Song He, Jinsong Su. *email: boxiaoc@163.com; hes1224@163.com; jssu@xmu.edu.cn.

21 absorbs local and global information and potential association information. In the application of
22 the cell line-specific drug-target heterogeneous graph, DTGRN significantly outperforms the
23 state-of-the-arts and several classical machine learning algorithms. More prominently, the novel
24 drug combinations predicted by DTGRN have been validated by computational analysis and in
25 vitro experiments, confirming the high predictive performance of DTGRN. These drug
26 combinations could be further evaluated as potential combination therapy strategy. In summary,
27 these results indicate that DTGRN can serve as a powerful tool for integrating heterogeneous
28 graph information to predict drug combinations and provide a promising way to discover novel
29 synergistic drug combination for cancer treatment.

30 **Introduction**

31 In recent decades, a deep understanding of tumor pathogenesis has facilitated the
32 development of anticancer drugs. However, due to the biological complexity of tumors, they often
33 develop resistance to monotherapy¹⁻³. To prevent and overcome drug resistance, combination
34 therapy has been proposed as a promising therapy⁴⁻⁷. Combination therapy has significant
35 advantages over monotherapy. It may slow down the drug resistance by affecting multiple targets
36 or pathways, and may reduce the toxicity of drugs due to the lower dosages used in
37 combination⁸⁻¹⁰. For many diseases, including cancers, synergistic drug combinations are often
38 more effective.

39 High-throughput screening accelerates the identification of novel synergistic drug
40 combinations¹¹. Relying on these large-scale screening methods, many available drug combination
41 data have been obtained, and then several databases have been constructed to collect the
42 combination screening data, such as DrugComb¹², SYNERGxDB¹³, and DCDB¹⁴. However, it is

43 impractical to screen all the drug combinations because of the large number of potential drug dose
44 combinations¹⁵⁻¹⁷. Thus, computational methods are urgently needed to predict potential
45 synergistic drug combinations based on available drug combination data.

46 In the past few years, many computational methods have been developed for drug
47 combination prediction, including network-based methods^{18,19}, mathematical methods²⁰, stochastic
48 search algorithms²¹, and machine learning methods²²⁻²⁷. Especially, with the wide use of deep
49 learning in many fields of drug discovery, some researchers have developed novel deep learning
50 methods to predict synergistic drug combinations²⁸⁻³¹. The deep learning methods with excellent
51 prediction performance are mainly based on deep neural networks (DNNs). For instance, Preuer *et al.*
52 *al.* proposed DeepSynergy²⁸, a feedforward neural network with two hidden layers. Chemical
53 descriptors were used as feature data of each drug, and gene expression values were used to
54 represent cancer cell lines. Kuru *et al.* applied three sub-neural networks to construct
55 Matchmaker²⁹. The chemical structure features of each drug were concatenated with gene
56 expression values of the corresponding cancer cell line and input to two subnetworks, respectively.
57 Then, the representations learned by the two subnetworks were concatenated and input to a third
58 subnetwork to predict the synergy scores. Both methods had good performance in classification
59 and regression tasks. However, these methods only use structural and physicochemical
60 information to represent drugs, while biological information is also necessary for combination
61 therapy. On the other hand, combination therapy may reduce the drug resistance due to targeting
62 multiple targets. Thus, the target-related information may be helpful in drug combination
63 prediction and the use of graph neural network (GNN) technologies to integrate drug-target
64 heterogeneous graph information is a promising strategy. Jiang *et al.* proposed a Graph

65 Convolutional Network (GCN) model to predict drug synergy in cancers by performing graph
66 embedding from an integrated drug-target interaction graph³¹. However, the GCN cannot fully
67 exploit heterogeneous graph by decomposing the graph into multiple subgraphs, processing them
68 separately, and then summing the outputs simply. As a result, the potential of the heterogeneous
69 graph has not been leveraged. In addition, for each kind of edge in heterogeneous graph, a large
70 number of parameters need to be added to the GCN, which brings difficulties to the training of the
71 model. Therefore, it is worthwhile to explore a more appropriate GNN technology for drug
72 combination prediction.

73 In this study, we proposed a Graph Recurrent Network (GRN) for the prediction of the
74 synergy effect of drug combinations, namely Drug-Target Graph based Recurrent Network
75 (DTGRN). DTGRN not only employs molecular fingerprints (MF) and physicochemical features
76 (PF) of drugs, structural and physicochemical features (SP) of drug targets, but also integrates
77 topological information from heterogeneous biological graphs. DTGRN employs gating
78 mechanism to dynamically determine the contribution weights of different types of neighbor
79 nodes and gate recurrent unit (GRU) for fewer parameters and better efficiency. Furthermore, in
80 addition to utilizing all node states, DTGRN introduces a cell-line-level state to fully integrate
81 heterogeneous graph information and learns node representation through continuous iteration.
82 Through this iterative encoding process, each drug node absorbs rich local and global information.
83 The final node representations learned by DTGRN are low-dimensional but informative
84 representations for drugs. Based on the final representations of drug nodes, DTGRN can predict
85 the synergy scores of drug combinations on a given cancer cell line and find novel synergistic
86 drug combinations. Validated on a variety of metrics, DTGRN shows significant performance

87 improvement compared to state-of-the-art drug combination prediction methods and several
88 advanced classical machine learning algorithms. We have also showed that adding additional
89 graphs (drug-target interaction (DTI) graph and protein-protein interaction (PPI) graph) can
90 improve the prediction performance. Furthermore, computational analysis and in vitro
91 experiments validated several novel drug combinations predicted by DTGRN.

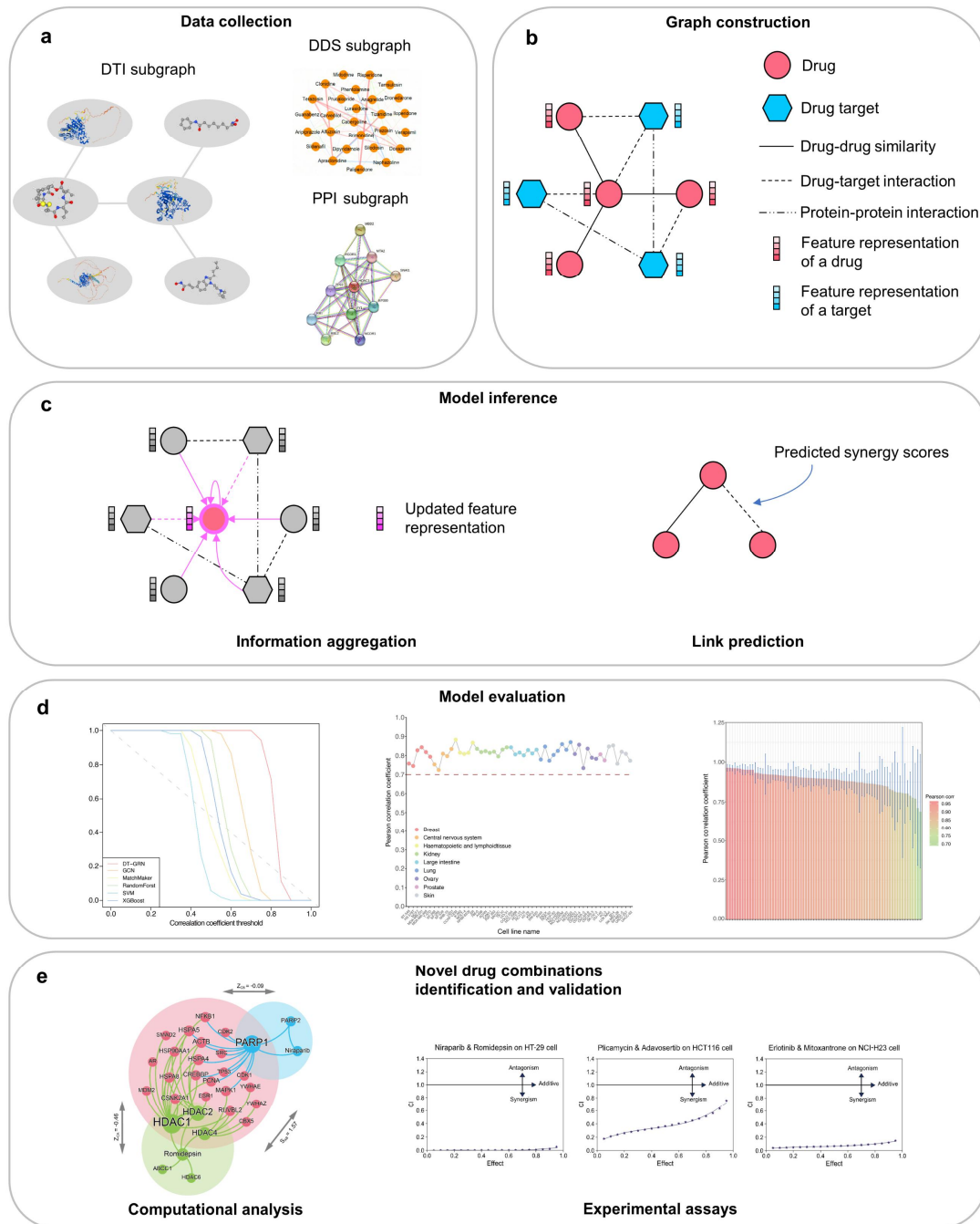
92 With excellent prediction performance, DTGRN can serve as a powerful tool for integrating
93 heterogeneous graph information to predict novel synergistic drug combinations. In general, we
94 characterize the following contributions of DTGRN: (1) We leveraged the topological features of
95 the heterogeneous graph and proved that the addition of DTI and PPI can improve the prediction
96 performance. Moreover, structural and physicochemical features were added as the drug nodes'
97 initial embeddings, leading to better performance. (2) To overcome the shortcomings of GCN, we
98 developed DTGRN, which significantly outperformed the state-of-the-arts. To the best of our
99 knowledge, our work is the first one to explore GRN for drug combination prediction. In DTGRN,
100 gating mechanism was employed to dynamically determine the contribution weights of different
101 types of neighbor nodes, GRU was employed for fewer parameters and better efficiency.
102 Furthermore, in addition to using all node states, we innovatively deployed a cell-line-level state
103 to fully integrate heterogeneous graph information. In this way, through an iterative encoding
104 process, the final embedding representation of the drug can more comprehensively capture rich
105 local and global information as well as potential association information. (3) The novel drug
106 combinations predicted by DTGRN have been validated by computational analysis and in vitro
107 experiments.

108 **Results**

109 **The framework of DTGRN**

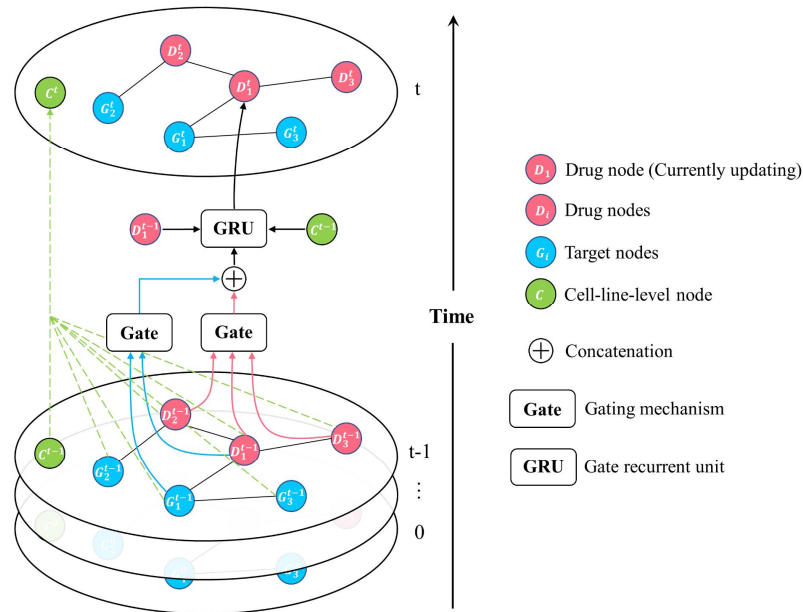
110 The framework of this study is depicted in Fig. 1. Firstly, for each cancer cell line, we
111 constructed three different types of subgraphs: drug-drug similarity (DDS) subgraph,
112 protein-protein interaction (PPI) subgraph, and drug-target interaction (DTI) subgraph. Then, the
113 DDS subgraph and PPI subgraph were connected according to DTI to construct a heterogeneous
114 graph. The drug molecular fingerprints (MF) were concatenated with drug physicochemical
115 features (PF) and then employed as the initial embeddings of the drug nodes, and the structural
116 and physicochemical features (SP) of target proteins were used as the initial embeddings of the
117 target nodes. As a result, we obtained 53 cell line-specific heterogeneous graphs. In the third part,
118 DTGRN took cell line-specific heterogeneous graphs as input and outputted the updated feature
119 representation for each node. DTGRN is a kind of graph recurrent network based on a message
120 passing framework for cell line-specific drug combination prediction. In the message passing
121 process, the update process of each node involved three key parts: the message was first collected
122 from its adjacent nodes, and then was used to update the node state by recurrent gating
123 mechanisms. Meanwhile, a cell-line-level state provided global information for the updates of
124 each node. Finally, after recurrent state transitions of several iterations, the updated feature
125 representation of the drug node was regarded as the final embedding representation and used to
126 predict synergy scores of drug combinations for the corresponding cell line. The details of
127 DTGRN are elaborated in the Methods section and Fig. 2. The fourth part is aimed at a
128 comprehensive performance evaluation of DTGRN, using a ROC-like curve, three metrics for
129 regression performance evaluation, and four metrics for classification performance evaluation.

130 The prediction performances for each specific tissue and each individual drug were evaluated, and
 131 the factors affecting model performance were further explored. Finally, novel drug combinations
 132 were identified by DTGRN and evaluated by computational analysis and in vitro experimental
 133 assays.
 134



135
 136 Fig. 1 The framework of this study. **a** Given a cancer cell line, three different types of subgraphs were constructed.
 137 **b** DDS subgraph and PPI subgraph were connected according to DTI to construct a heterogeneous graph. Drugs'

138 and targets' features were employed as the initial embeddings of each node. **c** DTGRN was trained to predict the
 139 synergy scores of drug combinations. **d** The ten-fold cross-validation was employed to evaluate the performance of
 140 DTGRN. Prediction performance across cell lines, tissues, and drugs was evaluated. **e** The computational analysis
 141 and experimental assays were performed to verify the novel predicted drug combinations.



142
 143 Fig. 2 DTGRN encoding for the drug-target heterogeneous graph. For the currently updating drug node, the
 144 message is collected from itself, its adjacent nodes, and cell-line-level state, and then is used to update the drug
 145 node state by recurrent gating mechanisms. Meanwhile, the cell-line-level state is updated by using the global
 146 topological features of the whole graph.

147 Comparison of DTGRN and previous methods

148 To demonstrate the superiority of DTGRN, we compared the performance of the proposed
 149 model with several classic and state-of-the-art methods, including Graph Convolutional Network³²,
 150 Deep Neural Network³³, Random Forest³⁴⁻³⁷, XGBoost³⁸, and SVM³⁹.

151 The performance of DTGRN was based on 10-fold cross-validation and was evaluated by
 152 three metrics: Pearson correlation coefficient, Spearman rank correlation coefficient, and R^2 . Tab.
 153 1 tabulates the mean and standard deviation of all cell lines for different metrics and for different
 154 methods. Furthermore, a ROC-like curve is defined as described in study⁴⁰ by setting a threshold
 155 Pearson r and plotted fraction ($r > r_{threshold}$). This ROC-like curve simplifies the understanding

156 of the fitting for those who are familiar with ROC⁴⁰. Fig. 3a shows the ROC-like curve of the cut
 157 correlated fraction versus the threshold Pearson r .

158 As shown in Tab. 1, DTGRN achieves the best performance compared to other methods and
 159 the improvements over the second-best method vary from 14% to 22% in these metrics.
 160 Particularly, DTGRN outperforms the state-of-the-art GCN-based method and the state-of-the-art
 161 DNN-based method, Matchmaker. More specifically, DTGRN achieves the highest Pearson
 162 correlation coefficient, 0.81, while the second-best method, GCN, has a Pearson correlation
 163 coefficient of 0.66. Of all the methods, SVM performs worst, yielding the lowest Pearson
 164 correlation coefficient of 0.43. In terms of the R^2 and Spearman rank correlation coefficient, we
 165 observed a similar trend.

166 Tab. 1 Performance evaluation in three metrics.

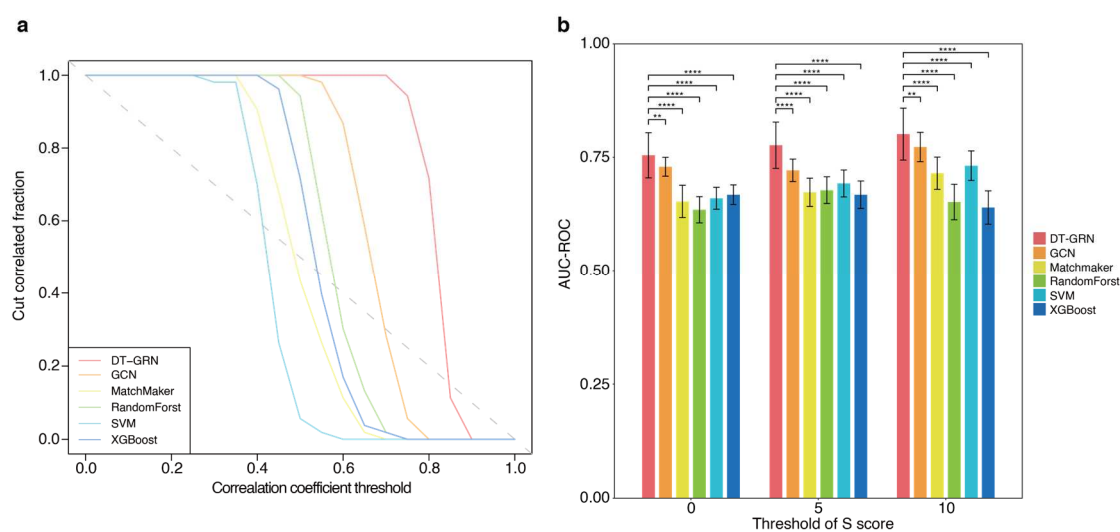
Performance metrics	Pearson		Spearman		R2	
	mean	std	mean	std	mean	std
DTGRN	0.8118	0.0346	0.7491	0.0435	0.6539	0.0559
GCN	0.6602	0.0569	0.6008	0.0506	0.4346	0.0743
MatchMaker	0.4947	0.0786	0.4316	0.0676	0.2483	0.0801
RandomForest	0.5672	0.0595	0.5355	0.0511	0.3171	0.0697
XGBoost	0.5298	0.0673	0.4957	0.0586	0.2320	0.0909
SVM	0.5166	0.0698	0.4918	0.0565	0.2435	0.1015

167

168 In order to assess the model’s ability to identify synergistic drug combinations, we further
 169 mimicked a binary classification task for evaluation. In this study, the S score was employed to
 170 reflect the strength of the synergistic/antagonistic effect. The density distribution of the S score is
 171 shown in Supplementary Fig. 1. According to the definition, the S scores greater than 0 indicate

172 the synergistic effect. However, drug combinations exhibiting a highly synergistic effect are
 173 attractive candidates for clinical studies⁴¹. Therefore, in this study, drug combinations with the
 174 actual S score higher than a threshold, m , are classified as positive (synergistic drug
 175 combinations), where $m \in (0,5,10)$. The drug combinations with the S score less than m belong
 176 to the negative class (non-synergistic drug combinations). For the classification performance
 177 evaluation, we used four metrics: accuracy (ACC), the area under the receiver operating
 178 characteristic curve (AUC-ROC), the area under the precision-recall curve (AUC-PR), and kappa
 179 score.

180 As indicated in Fig. 3b and Supplementary Fig. 2, when m varies, DTGRN still outperforms
 181 other approaches in this binary classification task. When m is set to 10, DTGRN, GCN,
 182 Matchmaker, and SVM methods have the optimal performance. This suggests that when the
 183 threshold of the S score is set to 10, the synergistic drug combinations and non-synergistic drug
 184 combinations are relatively easier to distinguish. When m is set to 0, the true positive and true
 185 negative may be mixed by noise.



186
 187 Fig. 3 Performance evaluation for the regression task and the binary classification task. **a** The ROC-like curve of
 188 the cut correlated fraction versus the threshold Pearson r . **b** AUC-ROC of all methods in the three thresholds of S
 189 scores. The x-axis denotes three thresholds, and the y-axis denotes the value of AUC-ROC. The bars indicate the

190 average of all cell lines' AUC-ROC and the lines on the bars represent the standard deviation. (Note: *: P
191 value \leq 0.05; **: P value \leq 0.01; ***: P value \leq 0.001; ****: P value \leq 0.0001.)

192 **Factors affecting the performance of DTGRN**

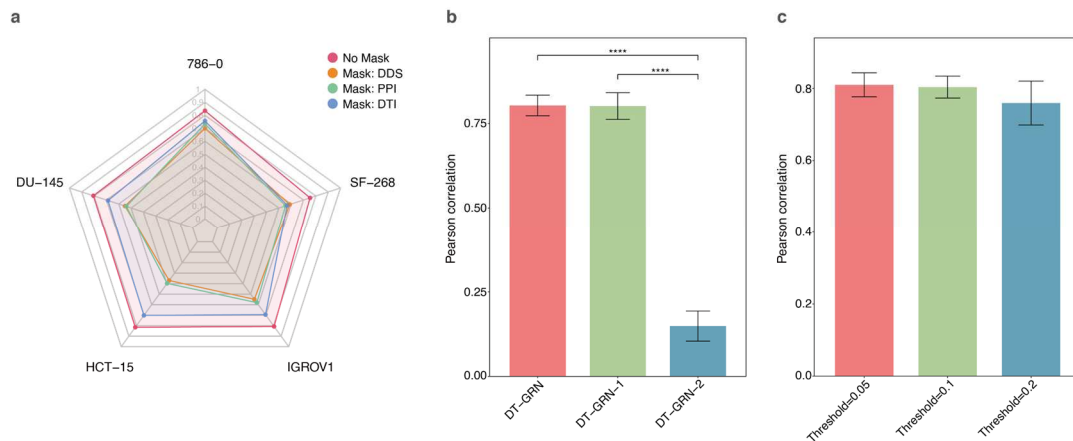
193 DTGRN is based on a heterogeneous graph that consists of a DDS subgraph, PPI subgraph,
194 and DTI subgraph. The performance of the model may be affected by various factors such as
195 graph structure, initial embeddings of drug nodes, and the threshold used to binarize the DDS
196 subgraph. Therefore, we analyzed the influencing factors for the model performance. To avoid
197 excessive time consumption, we selected five cancer cell lines from five different tissues for the
198 following experiments.

199 First of all, in order to demonstrate the rationality and importance of the existence of the
200 graph structure of each part in the heterogeneous graph, we removed the DDS, PPI, and DTI
201 respectively, and observed the changes in the model performance. The results are shown in Fig. 4a
202 and Supplementary Fig. 3a. The lack of any graph structure keeps the model from reaching peak
203 performance. That's, each subgraph in DTGRN gives its own contribution.

204 After that, for the DDS subgraph, we analyze the effect of different drug similarity
205 measurements and initial embeddings of drug nodes on the model performance. In our model, we
206 constructed DDS based on PF, and used MF and PF as the initial embeddings of the drug nodes.
207 Two auxiliary models (Tab. 2) were designed and compared with the original one (DTGRN). And
208 the performance of these three models is shown in Fig. 4b and Supplementary Fig. 3b. In the
209 auxiliary model DTGRN-1, DDS was constructed based on MF while the initial embeddings of
210 the drug nodes remained unchanged. No significant difference was observed between the
211 performances of DTGRN and DTGRN-1. In DTGRN-2, DDS was constructed based on PF and
212 the initial embeddings of the drug nodes were random initialization vectors. The performance of

213 DTGRN-2 was much worse than the performance of DTGRN. According to the performance of
 214 these models, DDS can be constructed based on PF or MF, but MF and PF must be employed as
 215 the initial embeddings of the drug nodes.

216 Subsequently, the threshold, t , used to binarize the DDS subgraph was tested. Here, t was
 217 set to ensure that 5%, 10%, and 20% of all the drug nodes were connected to the current node,
 218 respectively. When $t = 5%$ and $t = 10%$, there was no significant difference in the
 219 performance. When $t = 20%$, the performance degradation was observed (Fig. 4c and
 220 Supplementary Fig. 3c). Here, we set $t = 10%$ in DTGRN.



221
 222 Fig. 4 Factors affecting the performance of DTGRN. **a** Pearson correlation coefficient comparison before and after
 223 the DDS, PPI, and DTI mask in five different cell lines. **b** Pearson correlation coefficient of DTGRN and other two
 224 auxiliary models. **c** Pearson correlation coefficient of DTGRN in which the threshold, t , used to binarize the DDS
 225 subgraph was set to 0.05, 0.1 and 0.2.

226 Tab. 2 The configurations of auxiliary models

Abbreviation	Characteristics
DTGRN	DDS based on PF; Initial embeddings of the drug nodes: MF and PF
DTGRN-1	DDS based on MF; Initial embeddings of the drug nodes: MF and PF
DTGRN-2	DDS based on PF; Initial embeddings of the drug nodes: random initialization vector

227 **Cell line-specific drug combination prediction**

228 To investigate the model performance across cell lines, we calculated the prediction
229 performance metrics for 53 cell lines.

230 As shown in Supplementary Fig. 4, the Pearson correlation coefficient for the analyzed cell
231 lines ranges from 0.72 to 0.88 (using the 10-fold cross-validation method) with the mean of 0.81,
232 and the Spearman rank correlation coefficient ranges from 0.62 to 0.85 with the mean of 0.75.
233 Most cell line-specific DTGRN models performed consistently in terms of Pearson correlation
234 coefficient and Spearman rank correlation coefficient. For all cell lines, the Pearson correlation
235 coefficient was above 0.7, for 46 out of the 53 cell lines, the Spearman rank correlation coefficient
236 was above 0.7, indicating that DTGRN achieved good prediction performance for most of the cell
237 lines. The frequency distribution of the Pearson correlation coefficient and Spearman rank
238 correlation coefficient is shown in Supplementary Fig. 5. We further examined whether the cell
239 lines' predictive performance correlated with the number of drug-drug pairs for training. The
240 result shows that there is no correlation (Supplementary Fig. 6).

241 **Prediction performance across tissues and drugs**

242 To explore the varied performance, we further evaluated the prediction performance for each
243 specific tissue and each individual drug, respectively.

244 In the nine tissues consisting of 53 cell lines, the median of the Pearson correlation
245 coefficients was 0.81 for breast, 0.80 for central nervous system, 0.81 for haematopoietic and
246 lymphoid tissue, 0.82 for kidney, 0.82 for large intestine, 0.83 for lung, 0.80 for ovary, 0.79 for
247 prostate, and 0.81 for skin (Fig. 5a). DTGRN achieved a high Pearson correlation coefficient with
248 a small variance in lung (median, 0.83) and kidney (median, 0.82). In tissue-wise aspects, the

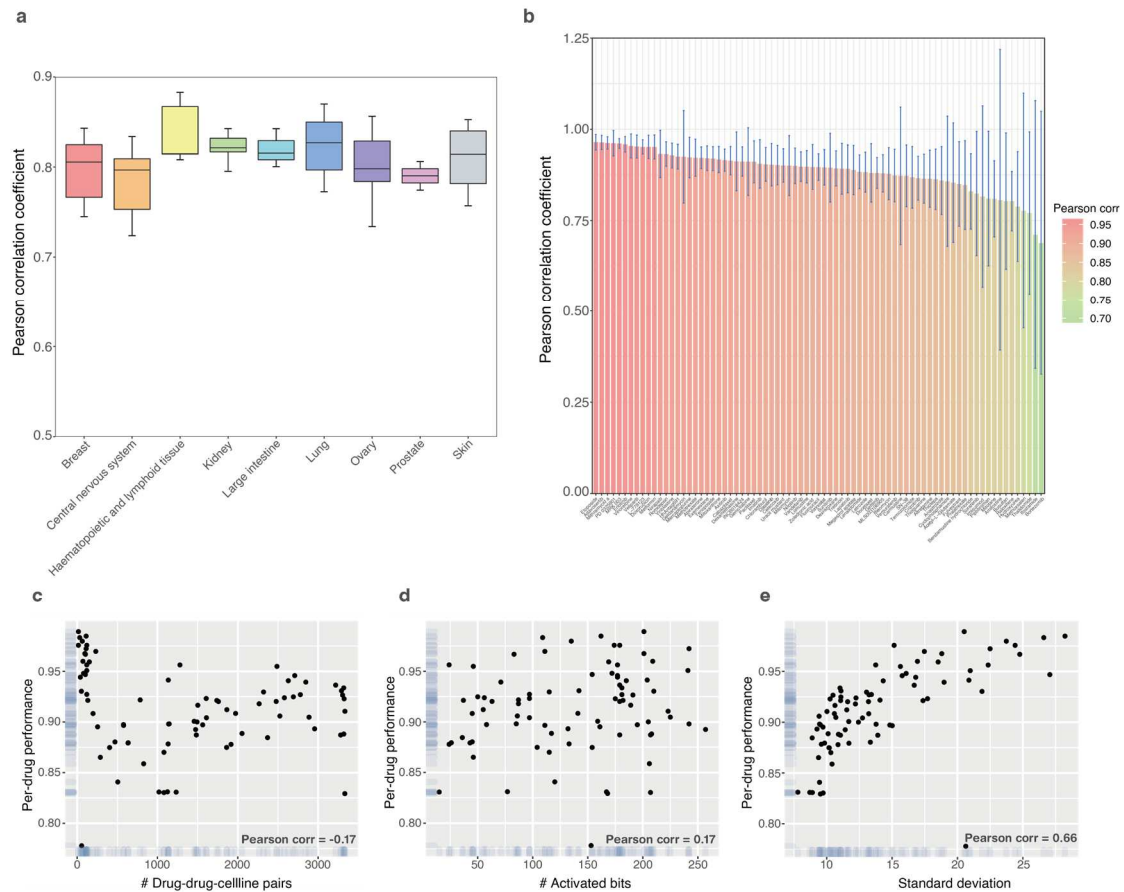
249 performance of DTGRN didn't vary intensely. This suggests that DTGRN which can be
250 introduced to different tissues has generalization power.

251 In drug-wise aspects, DTGRN achieved good prediction performance (Pearson correlation
252 coefficient was larger than 0.8) for more than 85% of drugs (Fig. 5b). For each individual drug,
253 the Pearson correlation coefficient was averaged across all cell lines and existing drug
254 combinations³².

255 Drugs with high Pearson correlation coefficients are more reliable in drug combination
256 therapy. For example, Etoposide, used for treatment of various types of cancers, including
257 refractory testicular tumors, small cell lung cancer, ovarian cancer, glioblastoma multiforme,
258 lymphoma, and non-lymphocytic leukemia, has the highest Pearson correlation coefficient.
259 According to previous studies, Etoposide is often used in combination with a variety of drugs. For
260 example, the combination of Etoposide and Cisplatin is highly effective and well-tolerated in
261 advanced thymoma⁴², the combination of Etoposide, Bleomycin, and Cisplatin is used in first-line
262 treatment for patients with disseminated germ cell cancer^{43,44}, the combination of Etoposide and
263 Temozolomide is a feasible candidate for the treatment of relapsed osteosarcoma⁴⁵, the
264 combination of Etoposide and Bevacizumab is safe and clinically active in a selected group of
265 patients with malignant gliomas⁴⁶, and Etoposide combined with FLAG salvage therapy is
266 effective in multiple acute myeloid leukemia⁴⁷.

267 We further examined whether the difference in the drugs' predictive performance arises from
268 (1) the different numbers of training data points, (2) the structural complexity of a drug (number
269 of activated bits), and (3) the specificity of a drug, which is quantified by the standard deviation of
270 the observed drug synergy scores across all drugs and cell lines. (Fig. 5c-e). (1) and (2) did not

271 show a clear association with performance. But we did find that drug performance strongly
 272 correlated with (3). This suggests that drugs possessing a larger range of synergy scores with
 273 different drugs on different cell lines (drugs with high specificity) tend to be more predictable.



274
 275 Fig. 5 **a** The Pearson correlation coefficient of DTGRN for different tissue types. **b** The Pearson correlation
 276 coefficient of DTGRN for different drugs. The bars indicate the average Pearson correlation coefficient across all
 277 cell lines and drug combinations. The lines on bars represent the standard deviation across all cell lines. **c**
 278 Scatterplot comparing the individual drugs' performance to the number of training data points. **d** Scatterplot
 279 comparing the individual drugs' performance to the structural complexity of the drug (number of activated bits). **e**
 280 Scatterplot comparing the individual drugs' performance to the standard deviation of the observed data points
 281 across all drugs and cell lines.

282 Identification of novel drug combinations

283 Next, we analyzed the novel drug combinations predicted by DTGRN, which are not
 284 included in the training data set. First of all, for each of the 53 cell lines, we selected the drug
 285 combination with the highest predicted S score for further validation, and a total of 53 drug

286 combinations (top 1 in each cell line) were obtained. Then, the drug combinations with S scores
287 less than 20 were removed. The remaining cell line-specific top 1 predictions are listed in
288 Supplementary Tab. 1. To further examine the reliability of these top predicted drug combinations,
289 an in-depth literature survey was performed, and 14 of 30 drug combinations have been reported
290 to show synergistic effects. For example, combination therapy of paclitaxel and sorafenib
291 enhances the efficiency compared to monotherapy according to the studies⁴⁸⁻⁵¹. Vemurafenib
292 combined with sorafenib was well-tolerated with encouraging activity in the clinical study⁵².

293 After that, we performed both computational analysis and in vitro experimental assays to
294 validate the novel predicted top 10 drug combinations in the HT-29, HCT116, and NCI-H23 cell
295 lines. In this section, we focus on the computational analysis results and will provide the in vitro
296 experimental results in the next section “In vitro experimental validation”.

297 We applied a network-based method to quantitatively measure the topological associations
298 between the novel predicted drug combinations and the disease-related genes in the PPI network.
299 In the study by Cheng *et al.*⁵³, they found that a drug combination had therapeutically synergistic
300 effects only if it was captured by the “Complementary Exposure” pattern, that is, the targets of the
301 drugs both hit the disease module, but target separate neighborhoods (Supplementary Fig. 7).
302 Relying on approved drug combinations for hypertension and cancer, they verified the
303 effectiveness of the method⁵³. In addition, the predictability of considering the topological
304 relations between drugs and disease-related genes in the PPI network was validated in some
305 related works⁵³⁻⁵⁵.

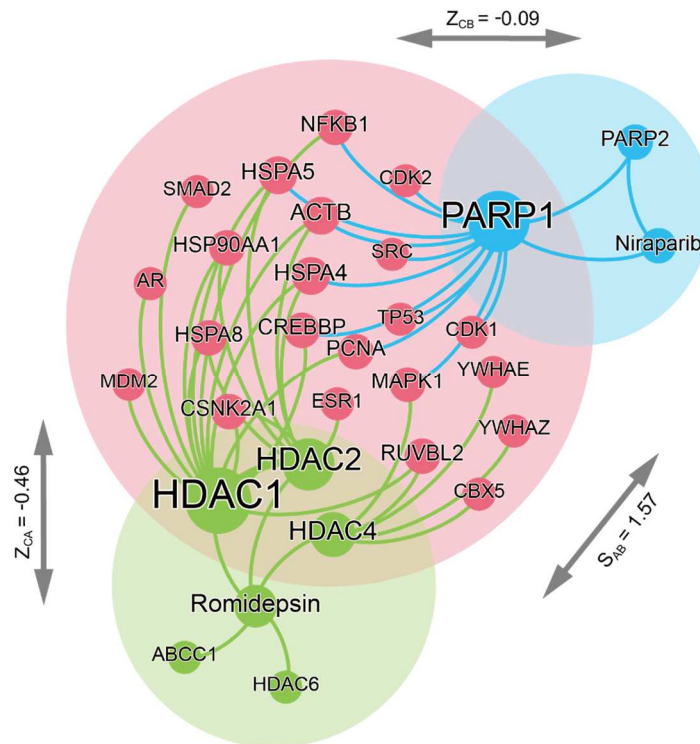
306 In this study, we employed the colon adenocarcinoma (COAD)-specific disease module
307 identified by GPSnet⁵⁶ (see methods) as the specific genes related to HT-29 and HCT116 cell lines

308 (two colon adenocarcinoma cell lines) in the PPI network, and lung adenocarcinoma
309 (LUAD)-specific disease module identified by GPSnet as the specific genes related to NCI-H23
310 cell line (a lung adenocarcinoma cell line) in the PPI network.

311 Supplementary Tab. 2 lists the topological associations of the top 10 drug combinations in
312 HT-29, HCT116, and NCI-H23 cell lines. Of the top 10 drug pairs in HT-29 (with a high S score),
313 except for one pair of drugs in which drug MRK-003 has no specific target gene, eight of the
314 remaining nine pairs were found to have a “Complementary Exposure” relationship to the
315 COAD-specific disease module (The ratio are 1/1 and 6/7 in HCT116 and NCI-H23 cell lines,
316 respectively). We showcased a drug combination in HT-29 (Niraparib & Romidepsin) in Fig. 6.

317 Niraparib is a poly-ADP ribose polymerase inhibitor (PARPi) used as an anti-cancer
318 medication. Inhibitors of nuclear PARPs are efficient therapeutics for several different types of
319 cancers⁵⁷. Unfortunately, a number of patients develop resistance to PARPi after long-term
320 administration⁵⁸. The combination of PARPi and histone deacetylase inhibitors (HDACi) is a
321 promising strategy and has been proved to sensitize PARPi-resistant cells to treatment⁵⁹⁻⁶⁴.
322 Furthermore, the combination of Niraparib and HDACi Romidepsin has been proved to have
323 synergistic effects in a previous study⁶⁵. The topological association in Fig. 6 may provide
324 important hints for understanding the underlying mechanisms of this synergistic effect.
325 Romidepsin is a natural cyclic peptide HDAC inhibitor. Inhibition of HDAC affects the
326 acetylation status and function of multiple non-histone proteins. It has been reported that MAPK1
327 (a member of the MAPK pathway) activities can be inhibited through HDAC inhibition⁶⁶.
328 Persistent activity of MAPK is related to PARPi resistance^{67,68}. Therefore, the modification of
329 MAPK by Romidepsin may be the reason why the combination of Niraparib and Romidepsin

330 enhances the efficacy of Niraparib.



331
332 Fig. 6 The inferred mode-of-action for the combination of Erlotinib and Romidepsin. The drug combination fits the
333 “Complementary Exposure” pattern and may have synergistic effect. Z_{CA} and Z_{CB} represent the network
334 proximity between disease-related gene module and targets (of drug A and B, respectively). S_{AB} represents the
335 proximity between modules of drug A and drug B.

336 **In vitro experimental validation**

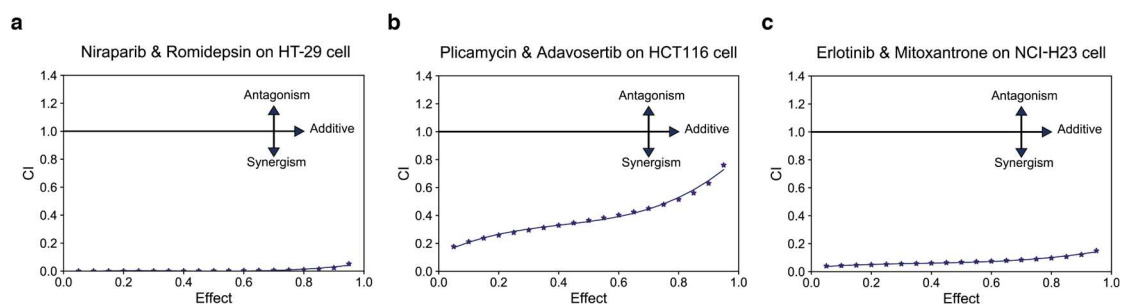
337 To further validate the ability of DTGRN to predict novel synergistic drug combinations, we
338 performed CCK-8 assay to examine the effects of drug combinations on cancer cell viability.
339 Based on the prediction results, the top 10 drug combinations in each of the three cancer cell lines
340 (HT-29, HCT116, and NCI-H23) with high predicted synergy scores were selected for the in vitro
341 experimental validation. Based on the dose-response values obtained by the CCK-8 assay, the
342 Combination Index (CI) of each drug combination was calculated by CompuSyn⁶⁹. Except for the
343 drugs that cannot be bought, a total of 25 possible drug combinations were used in the in vitro
344 experiment validation, of which 14 drug combinations were observed to have synergistic potential
345 (Tab.3, Fig. 7 and Supplementary Fig. 8-10). Fig. 7 demonstrates the most synergistic drug

346 combination of each cell line in the in vitro experimental validation.

347 Tab. 3 In vitro experimental validation of 25 possible drug combinations in HT-29, HCT116 and

348 NCI-H23 cell lines.

Cell line	Drug A	Drug B	Drug combinations validated by in vitro experiments
HT-29	Erlotinib	Gefitinib	
HT-29	Niraparib	Gefitinib	✓
HT-29	Erlotinib	Docetaxel	
HT-29	Erlotinib	Teniposide	✓
HT-29	Erlotinib	Romidepsin	
HT-29	Adavosertib	Gefitinib	
HT-29	Dexamethasone	Gefitinib	✓
HT-29	Niraparib	Romidepsin	✓
HT-29	Veliparib	Romidepsin	✓
HCT116	Dactolisib	Plicamycin	
HCT116	Adavosertib	Plicamycin	✓
HCT116	Erlotinib	Plicamycin	
HCT116	Niraparib	Plicamycin	✓
HCT116	Mirdametinib	Plicamycin	✓
HCT116	Vinblastine	Plicamycin	✓
HCT116	Erlotinib	Romidepsin	
HCT116	Veliparib	Plicamycin	
NCI-H23	Vinorelbine	Ifosfamide	✓
NCI-H23	Vinorelbine	Retinoic Acid	✓
NCI-H23	Vinorelbine	Erlotinib Hydrochloride	
NCI-H23	Erlotinib	Mitoxantrone	✓
NCI-H23	Erlotinib	Teniposide	✓
NCI-H23	Vinorelbine	Celecoxib	✓
NCI-H23	Vinorelbine	Nilotinib	
NCI-H23	Erlotinib	Ixabepilone	



349

350 Fig. 7 The experimental results of the most synergistic drug combinations in three cell lines. **a** Effect-CI plot of the
 351 combination of Niraparib and Romidepsin on HT-29 cell line. **b** Effect-CI plot of the combination of Plicamycin
 352 and Adavosertib on HCT116 cell line. **c** Effect-CI plot of the combination of Erlotinib and Mitoxantrone on
 353 NCI-H23 cell line.

354 In the HT-29 cell line, a canonical colorectal cancer cell line, five out of nine drug
 355 combinations (Niraparib & Gefitinib, Teniposide & Erlotinib, Romidepsin & Niraparib,
 356 Romidepsin & Veliparib, Dexamethasone & Gefitinib) were proved to have the potential of
 357 synergistic effect. We analyzed the possible action mechanisms of these drug combinations. For
 358 the drugs in these combinations, Niraparib, Erlotinib, and Gefitinib are indazole-based anticancer
 359 agents, which have been applied in the treatment of lung and colon cancers⁷⁰. It has been reported
 360 that epidermal growth factor receptor inhibitor (EGFRi) treatment can promote the sensitivity of
 361 peroxisome proliferator-activated receptor inhibitor (PARPi) and increase apoptosis levels in lung
 362 cancer⁷¹. The combination of PARPi Niraparib and EGFRi Gefitinib might inhibit cell
 363 proliferation by regulating DNA repair⁷² and EGFR/PI3K/AKT/mTOR pathway (Supplementary
 364 Fig. 8a). Teniposide, a chemotherapy medication for cancer, medicates topoisomerase⁷³ to inhibit
 365 cell cycle⁷⁴ and then suppresses cell proliferation. Teniposide combined with EGFRi Erlotinib
 366 suppresses cell proliferation via decreasing cell proliferation and increasing apoptosis⁷⁵ in the
 367 HT-29 cell line (Supplementary Fig. 8b). Wiegman *et al.* found that histone deacetylase inhibitor
 368 (HDACi) combined with PARPi is a novel strategy against cancer⁷⁶. Due to the HDACi
 369 Romidepsin induced apoptosis through the generation of hydrogen peroxide⁷⁷, the combination of

370 Romidepsin and PARP inhibitors Niraparib or Veliparib might increase cell apoptosis in HT-29
371 cell line⁷⁸ (Fig. 7a and Supplementary Fig. 8c). As an anti-proliferative and anti-inflammatory
372 drug, Dexamethasone involves in apoptosis and growth inhibition in colorectal cancer cell line⁷⁹.
373 Chemotherapy with Dexamethasone and Gefitinib might enhance chemosensitivity in colorectal
374 cancer via affecting inflammatory and cell apoptosis⁷⁵ (Supplementary Fig. 8d).

375 For another colorectal cancer cell line HCT116, the in vitro experiments confirmed that four
376 out of eight synergistic combinations (Plicamycin & Adavosertib, Plicamycin & Niraparib,
377 Plicamycin & Mirdametinib, Plicamycin & Vinblastine) have the potential of synergistic effect.
378 Plicamycin can decrease the expression of transcription factor specificity protein1 (Sp1), which is
379 involved in the cell cycle, apoptosis, and DNA damage, resulting in a treatment for colorectal
380 cancer^{80,81}. Inhibition of WEE1 G2 checkpoint kinase (WEE1) which can repair the DNA damage
381 is another attractive treatment strategy for colorectal cancer^{82,83}. By promoting DNA damage, the
382 WEE1 inhibitor Adavosertib may combine with Plicamycin to benefit colorectal cancer
383 treatment⁸² (Fig. 7b). Niraparib, a DNA repair inhibitor, can combine with Plicamycin to augment
384 DNA damage, resulting in cell apoptosis (Supplementary Fig. 9a). Mirdametinib can inhibit the
385 activity of MEK1 to decrease ERK2 phosphorylation and activation, thereby decreasing tumor cell
386 proliferation⁸⁴. Therefore, the combination of Mirdametinib and Plicamycin⁸⁵ effects the HCT116
387 cell line via inhibiting cell proliferation and promoting cell apoptosis (Supplementary Fig. 9b). As
388 a successful anti-tumor drug, Vinblastine is a microtubule-targeting vinca alkaloids that has used
389 in many chemotherapies. The combined therapeutic effects of Vinblastine and Plicamycin in the
390 HCT116 cell line are associated with a deregulation of the cell cycle^{86,87} (Supplementary Fig. 9c).

391 In the NCI-H23 cell line, five out of eight drug combinations (Vinorelbine & Celecoxib,

392 Vinorelbine & Ifosfamide, Vinorelbine & Retinoic acid, Erlotinib & Mitoxantrone, Erlotinib &
393 Teniposide) were evaluated to have synergistic effects. Vinorelbine, a semisynthetic vinca alkaloid,
394 could bind to tubulin to block mitotic progression⁸⁸, which represented a well-tolerated treatment
395 strategy for lung cancer⁸⁹. Cyclooxygenase 2 (COX-2) inhibitor Celecoxib regulates extrinsic
396 death receptor pathway to induce the apoptosis of lung cancer cell line⁹⁰. Similar to our
397 experimental result, clinical data has proved that the combination of Vinorelbine and Celecoxib
398 may benefit lung cancer treatment⁹¹ via accelerating apoptosis (Supplementary Fig. 10a).
399 Ifosfamide is an alkylating agent used in lung cancer treatment⁹² by inhibiting DNA synthesis to
400 induce cell death. Also, the combination of Vinorelbine and Ifosfamide has been demonstrated to
401 have a synergistic effect on the NCI-H23 cell line and has been used in lung cancer treatment^{93,94}
402 (Supplementary Fig. 10b). Retinoic acid, serving as a key role in cell proliferation^{95,96} through
403 inhibiting of cyclin D1 (CCND1), human telomerase reverse transcriptase (hTERT), epidermal
404 growth factor receptor (EGFR) and vascular endothelial growth factor (VEGF), is regarded as a
405 chemo-preventive agent for bronchogenic carcinoma. Recent studies have demonstrated that the
406 combination of Retinoic acid and the drugs for lung cancer treatment could decrease resistance
407 and enhance therapeutic efficacy^{97,98}. Therefore, the synergistic effects of Retinoic acid and
408 Vinorelbine in the NCI-H23 cell line might be associated with reduced resistance (Supplementary
409 Fig. 10c). Erlotinib is an EGFR inhibitor to promote DNA damage and Mitoxantrone can also
410 induce DNA damage through binding topoisomerase II and DNA in lung cancer cell line⁹⁹.
411 Because of the acceleration of DNA damage in NCI-H23 cell, the combination of Erlotinib and
412 Mitoxantrone showed a synergistic effect (Fig. 7c). In addition, the combination of Erlotinib and
413 Teniposide that was synergistic on the HT-29 cell line in our experiment was also detected a

414 synergistic effect on the NCI-H23 cell line. Combination therapy with Erlotinib and Teniposide
415 might show synergistic effect on the NCI-H23 by decreasing cell proliferation and increasing
416 apoptosis (Supplementary Fig. 10d).

417 In summary, the experimental results of the CCK-8 assays indicated that these drug
418 combinations could be further evaluated as potential combination therapy strategy. These
419 evidences also suggest strong support for the prediction of novel drug combinations by DTGRN,
420 and the potential of DTGRN to identify novel combinations deserves further exploration.

421 **Conclusion and Discussion**

422 The challenge in heterogeneous graph integration arises mainly from the heterogeneity and
423 complexity of data. In the field of drug combination prediction, drug-related graph integration is
424 also faced with the difficulty, and the great potential of GNN has not been fully exploited. The
425 existing GCN-based model faces the drawback that it is unable to fully exploit heterogeneous
426 graph by decomposing the graph into multiple subgraphs and processing them separately. In
427 addition, for each kind of edge in heterogeneous graph, a large number of parameters need to be
428 added to the GCN, which brings difficulties to the training of the model. Thus, it is worthy of
429 exploring a more appropriate GNN for drug combination prediction. In this paper, we proposed
430 DTGRN, a novel GRN method for predicting the synergy scores of drug combinations from
431 heterogeneous data sources. DTGRN characterizes the topology of heterogeneous graph
432 consisting of three subgraphs: DDS subgraph, PPI subgraph, and DTI subgraph. By integrating the
433 initial embeddings as well as global and local topological features, DTGRN obtains the drug
434 nodes' final representations used for drug combination prediction. We have demonstrated that
435 DTGRN outperforms both state-of-the-art deep learning model and GCN-based model (Tab. 1). In

436 addition, the computational analysis and in vitro experiments showed that DTGRN can identify
437 effective synergistic drug combinations by capturing the topological features of the heterogeneous
438 graph.

439 In this study, we used the topological features of DDS, as well as leveraged the topological
440 features of DTI and PPI. The synergistic effect between drugs is not only related to drugs' features
441 but also closely related to the features of their targets. Previous studies have shown that adding
442 drug targets' information can enhance the performance of models^{32,53,55}. According to the
443 experimental results, the addition of DTI and PPI can improve the prediction performance of
444 DTGRN, which fully demonstrates the effectiveness of drug targets' information for drug
445 combination prediction (Fig. 4a and Supplementary Fig. 3a).

446 In DTGRN, MF and PF are used as the initial embeddings of the drug nodes. Most studies
447 have applied the structural and physicochemical characteristics as the primary features of drugs.
448 When this type of feature is removed from DTGRN, the performance of the model decreases (Fig.
449 4b and Supplementary Fig. 3b). In addition to the structural and physicochemical characteristics,
450 the cell line-specific drug-induced gene expression profiles are also important features for model
451 training. However, if this type of feature is incorporated into DTGRN, the scale of the dataset will
452 be limited by the available gene expression profiles. In the future, with the accumulation of
453 drug-induced gene expression profiles, we expect that this information will be incorporated into
454 DTGRN and that the performance will be improved accordingly. Moreover, the growth of other
455 drug informatics data such as drug-disease relationships, drug-drug interactions, symptoms, and
456 drug side effects can be further exploited to enhance the model.

457 Next, both computational analysis and in vitro experimental validation were performed on

458 the novel predicted drug combinations, and the results preliminarily proved the predictive
459 performance of DTGRN. The computational analysis can also provide important hints for
460 understanding the underlying mechanisms of drug synergistic effect. Furthermore, 14 novel drug
461 combinations predicted by DTGRN were validated by in vitro experiments and can be further
462 evaluated as potential combination therapy strategies.

463 Although DTGRN shows excellent prediction performance, this study is faced with some
464 limitations. One limitation is that there are some noises and incompleteness in DTI and PPI. With
465 the completion of DTI and PPI in the future, a complete graph will be constructed and the
466 performance of DTGRN will be further improved. Another limitation is that drug pairs with high
467 synergy scores are not necessarily clinically effective drug combinations. The toxicities or side
468 effects of drug combination therapy, the effects of drug combinations on absorption, distribution,
469 metabolism, excretion (ADME), and the optimal dose range are also important factors affecting
470 the clinical application of drug combinations. In future research, these factors should be
471 incorporated and further explored.

472 In summary, DTGRN, a GRN-based model that utilizes heterogeneous graph information,
473 confirms its capability to serve as a general model for the identification of effective synergistic
474 drug combinations. The results showed that DTGRN outperforms the state-of-the-art drug
475 combination prediction methods and several advanced classical machine learning methods. By
476 effectively integrating the initial biological features as well as global and local topological features,
477 DTGRN can discover novel drug combinations. Impressively, several novel drug combinations
478 with high predicted scores have been validated to be effective by computational analysis and in
479 vitro experiments. While it is used to predict drug combinations, DTGRN is generalizable and

480 scalable for the integration of heterogeneous data sources and can be applied to predict other types
481 of relationships such as drug-target interactions and drug-drug interactions. Overall, by narrowing
482 the search space of drug combinations, DTGRN can be a valuable approach for the discovery of
483 novel synergistic drug combinations.

484 **Methods**

485 **Drug combination data set**

486 We collect drug combination data from DrugComb (v1.4), an integrative cancer drug
487 combination data portal¹⁰⁰. In this open-access data portal, the results of drug combination
488 screening studies (O’Neil *et al.* Study¹⁰¹, NCI-ALMANAC¹⁰², Forcina¹⁰³ and Cloud datasets¹⁰⁴)
489 are accumulated, standardized and harmonized. DrugComb contains 466,033 combinations for
490 4,101 drugs tested in 112 cell lines. It also provides 5 types of synergy scores for these
491 combinations, including Bliss independence (Bliss)¹⁰⁵, Highest single agent (HSA)¹⁰⁶, Loewe
492 additivity (Loewe)¹⁰⁷, Zero interaction potency (ZIP)¹⁰⁸, and a novel measure called S score.

493 To ensure the quantity and quality of training data in each cell line, we remove the cell lines
494 that contained less than 5,000 drug pairs or less than 10% drug pairs with S scores greater than
495 zero. We then obtain 335,692 drug combination experiments across 53 cell lines. For some drug
496 pairs, there are more than one replicate experiments reporting synergy scores. Therefore, in this
497 study, synergy scores in replicate experiments are averaged to get a unique value for each drug
498 combination in each cell line. Finally, we obtain 33,014 drug combinations across 53 cell lines.

499 **Synergy score**

500 In this study, the S score is used as the quantitative measurement of the synergistic effect of
501 drug combinations, which is introduced along with the DrugComb database^{100,109}. The S score is

502 developed based on the differences between the dose-response curves of a drug combination and
503 its single drug in cross-design experiments. According to the criteria of all the four existing
504 synergy scoring models (HSA, Bliss, Loewe and ZIP), Malyutina *et al.* proved that the S score can
505 predict the most synergistic and antagonistic drug combinations with high accuracy
506 (AUC-ROC>0.99)¹⁰⁹. According to the definition of the S score, an S score greater than 0 or less
507 than 0 indicates the synergistic effect or antagonistic effect, respectively. And the greater the S
508 score, the stronger the synergistic effect.

509 **Drug-target interaction**

510 The drug-target interaction data is extracted from the DrugBank database, a bioinformatics
511 resource with detailed drug data and complete drug target interaction data¹¹⁰. We obtain a total of
512 8,083,600 interactions between 500,000 drugs and 8,900 target proteins.

513 **Protein-protein interaction**

514 We use the comprehensive human PPI network generated by Menche *et al.*¹¹¹, which is
515 integrated from seven sources of protein interactions. The PPI network contains a total of 13,460
516 proteins that are interconnected by 141,296 interactions.

517 **Drug molecular fingerprint and similarity measurement**

518 For each drug d , we first extract the chemical structure data in the SDF format from the
519 PubChem Compound database¹¹², which contains more than 92 million unique structures of
520 compounds.

521 Then we use the *R* package “ChemmineR” to encode each drug into an 881-dimensional
522 chemical substructure vector defined in PubChem¹¹³. That is, each drug d is represented by a
523 binary fingerprint $E(d)$ in which each bit indicates the presence of a predefined chemical

524 structure fragment.

525 The pairwise chemical similarity between two drugs d_1 and d_2 is calculated as the
526 Tanimoto coefficient of their fingerprints:

$$S_{d_1, d_2}^{MF} = \frac{E(d_1) \times E(d_2)}{|E(d_1)| + |E(d_2)| - E(d_1) \times E(d_2)} \quad (1)$$

527 where $|E(d_1)|$ and $|E(d_2)|$ are the counts of structure fragments for drug d_1 and d_2 ,
528 respectively, and $E(d_1) \times E(d_2)$ represents the number of the structure fragments shared by the
529 two drugs.

530 **Drug physicochemical feature and similarity measurement**

531 The physicochemical properties represent the physical and chemical properties of drugs.
532 These properties of drugs play an important role in the discovery of potential drug candidates
533 ¹¹⁴⁻¹¹⁶.

534 In this study, we extract each drug's 102 physicochemical (i.e., polar surface area, molar
535 refractivity, and molecular weight) descriptors, which are quantitated based on the Pybel¹¹⁷,
536 JOELib2¹¹⁸, and ChemmineR chemoinformatics tools¹¹³. We calculate similarity based on
537 physicochemical feature between drugs d_1 and d_2 as the cosine similarity of the descriptors:

$$S_{d_1, d_2}^{PF} = \frac{\vec{d}_1 \cdot \vec{d}_2}{\|\vec{d}_1\| \|\vec{d}_2\|} \quad (2)$$

538 where \vec{d}_1 and \vec{d}_2 are 102-dimensional feature vectors of drugs d_1 and d_2 , respectively, and
539 $\|\vec{d}_1\|$ and $\|\vec{d}_2\|$ represent the norms of feature vectors of drugs d_1 and d_2 , respectively.

540 **Structural and physicochemical features of drug target**

541 Protein sequence-derived structural and physicochemical features are very helpful for
542 distinguishing proteins of different functional properties and have been frequently used for
543 analyzing and predicting various profiles of proteins¹¹⁹. In this study, we first extract protein

544 sequence data from the UniProt database, which provides high-quality and freely accessible
545 protein sequence data¹²⁰. Next, the protein features are generated by using PROFEAT, a web
546 server for computing the structural and physicochemical descriptors of proteins from amino acid
547 sequence^{119,121-123}. The computed features include 1437 descriptors such as amino acid
548 composition, Moran autocorrelation, Hydrophobicity, etc.

549 **Cell line-specific heterogeneous graph construction**

550 For each cell line, a heterogeneous graph is constructed based on three types of subgraphs:
551 DDS subgraph, DTI subgraph, and PPI subgraph. First, we binarize the DDS subgraph using a
552 synergy score t as the threshold for each cell line. Then, the drug-target associations are added to
553 the graph through the mapping of DTI. Finally, the PPI subgraph is mapped into the drug-target
554 heterogeneous graph. As a result, a total of 53 cell line-specific heterogeneous graphs are
555 established. For the target protein nodes in the heterogeneous graphs, structural and
556 physicochemical features of proteins are used as the initial embeddings. For the drug nodes in the
557 heterogeneous graphs, molecular fingerprints and physicochemical features are used as the initial
558 embeddings.

559 **Workflow of DTGRN**

560 According to the characteristics of data sets, we design a GRN for drug combination
561 prediction. Essentially, GRN is a type of GNN based on a message-passing framework, where
562 node states are updated iteratively by recurrent gating mechanisms such as LSTM and
563 GRU. Generally, at each message passing step, the update process of each node involves two
564 sub-steps. First, the message is collected from its adjacent nodes. Second, it is used to update the
565 node state by recurrent gating mechanisms.

566 Fig. 2 shows the message passing procedures of the DTGRN. In addition to node states in the
 567 graph, we introduce a cell-line-level state C , which collects global information for the updates of
 568 other nodes. Particularly, for different types of nodes, we apply separate encoding parameters and
 569 gating operations to model their state transition processes.

570 Concretely, at the t -th step, we update the state of the node using the weighted sum of the
 571 message from its neighboring heterogeneous node states and isomorphic node states. Formally, for
 572 the state update of the drug node d_i at step t , the message from its neighboring drug nodes states
 573 (such as $k_{d_j}^{(t-1)}$) and target nodes states (such as $k_{g_j}^{(t-1)}$) are collected as follows:

$$\begin{aligned} m_{d_i}^{(t)} &= \sum_{d_j \in N_d(d_i)} \alpha_{i,j} k_{d_j}^{(t-1)} \\ \tilde{m}_{d_i}^{(t)} &= \sum_{g_j \in N_g(d_i)} \beta_{i,j} k_{g_j}^{(t-1)} \end{aligned} \quad (3)$$

574 where $N_d(d_i)$ and $N_g(d_i)$ are neighboring drug and target nodes of d_i , respectively. The
 575 weights $\alpha_{i,j}$ and $\beta_{i,j}$ are calculated according to their edge types and associated node states,
 576 both of which are fed into a single-layer neural network with a sigmoid activation function. Then,
 577 we update the drug state $k_{d_i}^{(t)}$ by using $m_{d_i}^{(t)}$, $\tilde{m}_{d_i}^{(t)}$ and the cell-line-level state $C^{(t-1)}$ in the
 578 following way:

$$\begin{aligned} \xi_{d_i}^{(t)} &= [s_{d_i}; m_{d_i}^{(t)}; \tilde{m}_{d_i}^{(t)}; C^{(t-1)}] \\ r_{d_i}^{(t)} &= \sigma \left(W^r \xi_{d_i}^{(t)} + U^r k_{d_i}^{(t-1)} \right) \\ z_{d_i}^{(t)} &= \sigma \left(W^z \xi_{d_i}^{(t)} + U^z k_{d_i}^{(t-1)} \right) \\ u_{d_i}^{(t)} &= \tanh \left(W^u \xi_{d_i}^{(t)} + U^u \left(r_{d_i}^{(t)} \odot k_{d_i}^{(t-1)} \right) \right) \\ k_{d_i}^{(t)} &= \left(1 - z_i^{(t)} \right) \odot u_{d_i}^{(t)} + z_i^{(t)} \odot k_{d_i}^{(t-1)} \end{aligned} \quad (4)$$

579 where s_{d_i} is the initial embedding of drug node d_i , W^* and U^* ($* \in \{r, z, u\}$) denote trainable
 580 parameters. Similarly, the target state $k_{g_i}^{(t)}$ is updated based on $k_{g_i}^{(t-1)}$, its initial embedding s_{g_i} ,

581 its connected drug nodes and target nodes, and the cell-line-level state $C^{(t-1)}$.

582 Finally, we update the state of the cell-line-level node $C^{(t-1)}$ with the message from all drug

583 nodes and target nodes:

$$\begin{aligned}
\hat{k}_d^{(t-1)} &= \frac{1}{|V_d|} \sum_{m=1}^{|V_d|} k_{d_m}^{(t-1)} \\
\hat{k}_g^{(t-1)} &= \frac{1}{|V_t|} \sum_{m=1}^{|V_t|} k_{g_m}^{(t-1)} \\
r_c^{(t)} &= \sigma \left(W^{dr} \hat{k}_d^{(t-1)} + W^{gr} \hat{k}_t^{(t-1)} + U^{Cr} C^{(t-1)} \right) \\
z_c^{(t)} &= \sigma \left(W^{dz} \hat{k}_d^{(t-1)} + W^{gz} \hat{k}_t^{(t-1)} + U^{Cz} C^{(t-1)} \right) \\
u_c^{(t)} &= \tanh \left(W^{du} \hat{k}_d^{(t-1)} + W^{gu} \hat{k}_t^{(t-1)} + U^{Cu} (r_c^{(t)} \odot C^{(t-1)}) \right) \\
C^{(t)} &= \left(1 - z_c^{(t)} \right) \odot u_c^{(t)} + z_c^{(t)} \odot C^{(t-1)}
\end{aligned} \tag{5}$$

584 where W^* ($* \in \{dr, gr, dz, gz, du, gu\}$) and U^* ($* \in \{Cr, Cz, Cu\}$) denote trainable parameters,

585 and $|V_d|$, $|V_t|$ are the numbers of drug nodes and target nodes, respectively.

586 The above recurrent state transitions process is iterated T times. Afterwards, the final drug

587 states $k_d^{(T)}$ can be obtained, which is used to predict the synergy scores. Through this process,

588 each drug node absorbs rich local and global information and captures potential associated

589 information.

590 Finally, the synergy score s_{d_i, d_j} between drug nodes d_i and d_j is calculated from the final

591 drug node embeddings via the following bilinear form:

$$s_{d_i, d_j} = k_{d_i}^{(T)T} R_c k_{d_j}^{(T)} \tag{6}$$

592 where R_c stands for a cell line-specific projection matrix.

593 Network-based model for drug combinations

594 Network-based computational analysis is performed to measure the topological associations

595 between drug combinations and disease-related genes in the PPI network.

596 The network-based proximity between a drug module and a disease module is defined as
597 follows:

$$d(U, V) = \frac{1}{|U| + |V|} \left(\sum_{u \in U} \min_{v \in V} d(u, v) + \sum_{v \in V} \min_{u \in U} d(u, v) \right) \quad (7)$$

598 where U represents the set of genes related to a specific disease, and V represents the set of drug
599 targets. $|U|$ and $|V|$ are the size of the disease-related gene set and the drug target set,
600 respectively, and $d(u, v)$ is the shortest distance between gene u and v in the PPI network.

601 To assess the significance of the association, Z-score is defined based on permutation tests:

$$Z_{d(U, V)} = \frac{d(U, V) - \mu_p}{\sigma_p} \quad (8)$$

602 where μ_p and σ_p are the mean and standard deviation of a reference distance distribution, which
603 is generated by the permutation test repeated 1000 times. In each permutation test, two randomly
604 selected gene lists with similar degree distributions to those of U and V are utilized to calculate
605 the distance⁵⁴.

606 However, the Z-score is not suitable for measuring the proximity between two drug
607 modules⁵³. Therefore, a “separation” measure is defined:

$$S(X, Y) = \langle d(X, Y) \rangle - \frac{\langle d(X, X) \rangle + \langle d(Y, Y) \rangle}{2} \quad (9)$$

608 where $\langle d(X, X) \rangle$ and $\langle d(Y, Y) \rangle$ are the average shortest path length within the drug-target
609 module X and drug-target module Y , respectively. $\langle d(X, Y) \rangle$ is the average shortest path length
610 between drug-target module X and drug-target module Y (Calculate according to Eq. 3). For
611 $S(X, Y) > 0$, the targets of the two drugs are topologically separated.

612 **Specific genes related to cancer cell lines**

613 HT-29 and HCT116 cell lines are colon adenocarcinoma cell lines. Thus, the specific genes

614 related to HT-29 and HCT116 cell lines are represented by the COAD-specific disease module
615 identified by GPSnet⁵⁶. Similarly, the specific genes related to NCI-H23 are represented by the
616 LUAD-specific disease module identified by GPSnet. Genome-wide Positioning Systems network
617 (GPSnet) is a novel network-based disease module identification and in silico drug repurposing
618 methodology⁵⁶. Via GPSnet, we identify the COAD-specific disease modules with 168 genes and
619 LUAD-specific disease modules with 141 genes by integrating whole-exome sequencing and
620 transcriptome profiling into the human protein–protein interactome.

621 **Comparison algorithms and evaluation metrics**

622 To demonstrate the superiority of DTGRN, we compare the performance of DTGRN with
623 some classic and state-of-the-art baselines. The compared methods include GCN, DNN, Random
624 Forest, SVM, and XGBoost. The GCN-based model is a state-of-the-art GNN model for drug
625 combination prediction³². The Matchmaker is a state-of-the-art deep learning method for drug
626 combination prediction based on DNNs³³. And the three advanced classical machine learning
627 algorithms have also shown excellent performance in drug combination prediction³⁴⁻³⁹.

628 Random Forest, XGBoost, and SVM are implemented in scikit-learn or other python
629 modules with default settings¹²⁴⁻¹²⁷. The parameters of GCN and Matchmaker follow the
630 configurations proposed in the papers^{28,32,33,128}. The hyperparameters of DTGRN are listed in
631 Supplementary Tab. 3.

632 All algorithms are validated on the data set using 10-fold cross-validation. We employ the
633 Pearson correlation coefficient, Spearman rank correlation coefficient, and R^2 score as the
634 regression metrics, and reported the mean and the standard deviation. Pearson correlation
635 coefficient and Spearman rank correlation coefficient are widely used to measure the correlation

636 between the ground-truth labels and predictions (Eq. 10 and Eq. 11). R^2 indicates the extent to
 637 which the predictions of models outperform the average value (Eq. 12). Here \bar{y} is the average of
 638 y_i ($1 \leq i \leq m$), r_Y, r_y are the rank variables of Y and y , respectively. $cov(r_Y, r_y)$ is the
 639 covariance of the rank variables, and σ_{r_Y} and σ_{r_y} are the standard deviations of the rank
 640 variables.

$$pearson = \frac{\sum_{i=1}^m (Y_i - \bar{Y})(y_i - \bar{y})}{\sqrt{\sum_{i=1}^m (Y_i - \bar{Y})^2} \sqrt{\sum_{i=1}^m (y_i - \bar{y})^2}} \quad (10)$$

$$spearman = \frac{cov(r_Y, r_y)}{\sigma_{r_Y} \sigma_{r_y}} \quad (11)$$

$$R^2 = 1 - \frac{\sum_{i=1}^m (Y_i - y_i)^2}{\sum_{i=1}^m (Y_i - \bar{Y})^2} \quad (12)$$

641 Cell lines and cell culture

642 HT-29/HCT116/NCI-H23 cell lines used in this study are obtained from Procell Life Science
 643 & Technology. All cell lines are validated by STR profiling performed by Cell Line Authentication
 644 Service at ATCC. Cells are cultured in DMEM medium (#12440053, Gibco) or McCoy's 5A
 645 medium (PM150710, ProCell) or RPMI1640 (#SH30809, Hyclone) supplemented with 10% FBS
 646 (#10500064, Gibco) and penicillin–streptomycinx (#15070063, Gibco) at 37°C and 5% CO₂ in a
 647 humidified incubator.

648 Compounds

649 All drugs are solubilized in DMSO and stored at -20 °C. The list of drugs in this study is
 650 shown in Supplementary Tab. 4.

651 Drug combination screening

652 To evaluate the drug combination in three cell lines, a Cell Counting Kit-8 (CCK8) assay
 653 (Sigma, M5655) is performed. The drug combination testing experimental design is adopted from

654 Christian *et al.*⁶⁹. The concentration of drugs is set to 10 different values in the combination
655 testing experimental design (Supplementary Tab. 4). Cells are seeded in 96-well plates (Nest,
656 701001) at 4000 cells/well densities and cultured at the indicated concentrations with either the
657 solvent DMSO, drug combinations for 72 h. After 72 h of incubation, 10µl per well of CCK8
658 reagent is added to the plates, followed by 4 h of incubation. The luminescence of optical density
659 value (OD) is detected using an Envision plate reader (PerkinElmer) at the wavelength of 450nm.
660 The cellular proliferation inhibition rate is defined according to Eq. 13. Then the CI of drug
661 combination is calculated by CompuSyn software to quantify the synergism between drugs⁶⁹.

$$\text{inhibition (\%)} = \frac{(OD^{sample} - OD_{Negative})}{(OD_{Positive} - OD_{Negative})} \times 100\% \quad (13)$$

662

663 **Code availability**

664 The source code of the DTGRN algorithm is freely available at GitHub repository
665 <https://github.com/czwlines/DT-GRN> (ref. ¹²⁹) to allow replication of the results and to compare
666 DTGRN with other prediction models.

667

668 **Reference**

- 669 1 Jessica Vamathevan ¹, D. C., Paul Czodrowski ³, Ian Dunham ⁴, Edgardo
670 Ferran ², George Lee ⁵, Bin Li ⁶, Anant Madabhushi ⁷ ⁸, Parantu
671 Shah ⁹, Michaela Spitzer ⁴, Shanrong Zhao ¹⁰. Applications of machine learning
672 in drug discovery and development(Review). *Nature Reviews Drug Discovery* **Vol.18**,
673 463-477, doi:10.1038/s41573-019-0024-5 (2019).
- 674 2 Juanita S Lopez ¹, U. B. Combine and conquer: challenges for targeted therapy
675 combinations in early phase trials. *Nature Reviews Clinical Oncology* **Vol.14**, 57-66,
676 doi:10.1038/nrclinonc.2016.96 (2017).
- 677 3 Jia, J. *et al.* Mechanisms of drug combinations: interaction and network perspectives. *Nat*
678 *Rev Drug Discov* **8**, 111-128, doi:10.1038/nrd2683 (2009).
- 679 4 Chou, T.-C. Theoretical basis, experimental design, and computerized simulation of
680 synergism and antagonism in drug combination studies. *Pharmacological reviews* **Vol.58**,
681 621-681, doi:10.1124/pr.58.3.10 (2006).
- 682 5 Ianevski, A. *et al.* Prediction of drug combination effects with a minimal set of

683 experiments. *Nature machine intelligence* **Vol.1**, 568-577,
684 doi:10.1038/s42256-019-0122-4 (2019).

685 6 Dean, H. Artificial intelligence in cancer therapy. *Science (New York, N.Y.)* **Vol.367**,
686 982-983, doi:10.1126/science.aaz3023 (2020).

687 7 Holohan, C., Van Schaeybroeck, S., Longley, D. B. & Johnston, P. G. Cancer drug
688 resistance: An evolving paradigm(Review). *Nature Reviews Cancer* **Vol.13**, 714-726,
689 doi:10.1038/nrc3599 (2013).

690 8 Zimmermann, G. R., Lehár, J. & Keith, C. T. Multi-target therapeutics: when the whole is
691 greater than the sum of the parts. *Drug Discovery Today* **12**, 34-42,
692 doi:<https://doi.org/10.1016/j.drudis.2006.11.008> (2007).

693 9 Lukas, M. *et al.* Survey of ex vivo drug combination effects in chronic lymphocytic
694 leukemia reveals synergistic drug effects and genetic dependencies. *Leukemia*,
695 doi:10.1038/s41375-020-0846-5 (2020).

696 10 Tonekaboni, S., Ghoraie, L., Manem, V. & Haibe-Kains, B. Predictive approaches for drug
697 combination discovery in cancer. *BRIEFINGS IN BIOINFORMATICS* **Vol.19**, 263-276,
698 doi:10.1093/bib/bbw104 (2018).

699 11 Leh *et al.* Synergistic drug combinations tend to improve therapeutically relevant
700 selectivity. *Nature Biotechnology* **Vol.27**, 659-666, doi:10.1038/nbt.1549 (2009).

701 12 Zagidullin, B. a. *et al.* DrugComb: an integrative cancer drug combination data
702 portal(Article). *Nucleic Acids Res.* **Vol.47**, W43-W51, doi:10.1093/nar/gkz337 (2019).

703 13 Haibe-Kains, B. *et al.* SYNERGxDB: an integrative pharmacogenomic portal to identify
704 synergistic drug combinations for precision oncology. *Nucleic Acids Research* **48**,
705 W494-W501, doi:10.1093/nar/gkaa421 (2020).

706 14 Liu, Y., Hu, B., Fu, C. & Chen, X. DCDB: Drug combination database. *Bioinformatics* **26**,
707 587-588, doi:10.1093/bioinformatics/btp697 (2009).

708 15 Zhao, X.-M. *et al.* Prediction of Drug Combinations by Integrating Molecular and
709 Pharmacological Data. *PLoS Computational Biology* **7**, doi:10.1371/journal.pcbi.1002323
710 (2011).

711 16 Bleicher, K. H., Böhm, H.-J., Müller, K. & Alanine, A. I. Hit and lead generation: beyond
712 high-throughput screening. *Nature Reviews Drug Discovery* **2**, 369-378,
713 doi:10.1038/nrd1086 (2003).

714 17 Morris, M. K., Clarke, D. C., Osimiri, L. C. & Lauffenburger, D. A. Systematic Analysis of
715 Quantitative Logic Model Ensembles Predicts Drug Combination Effects on Cell Signaling
716 Networks. *CPT: Pharmacometrics & Systems Pharmacology* **5**, 544-553,
717 doi:10.1002/psp4.12104 (2016).

718 18 Cheng, F., Kovacs, I. A. & Barabasi, A. L. Network-based prediction of drug combinations.
719 *Nat Commun* **10**, 1197, doi:10.1038/s41467-019-09186-x (2019).

720 19 Roth, F. P. *et al.* Target Inhibition Networks: Predicting Selective Combinations of
721 Druggable Targets to Block Cancer Survival Pathways. *PLoS Computational Biology* **9**,
722 doi:10.1371/journal.pcbi.1003226 (2013).

723 20 Lee, J.-H. *et al.* CDA: Combinatorial Drug Discovery Using Transcriptional Response
724 Modules. *PLoS One*, 2012, doi:10.1371/journal.pone.0042573 (2012).

725 21 Zinner, R. G. *et al.* Algorithmic guided screening of drug combinations of arbitrary size
726 for activity against cancer cells. *Mol. Cancer Ther.* **Vol.8**, 521-532,

727 doi:10.1158/1535-7163.Mct-08-0937 (2009).

728 22 Li, P., Huang, C. & Fu, Y. Large-scale exploration and analysis of drug combinations.
729 *Bioinformatics* **Vol.31**, doi:10.1093/bioinformatics/btv080 (2015).

730 23 1, P. S., 2, S. N., Ariey-Bonnet, J., 2, E. P. & 2, P. B. Predicting Synergism of Cancer Drug
731 Combinations Using NCI-ALMANAC Data. *Frontiers in Chemistry* **Vol.7**,
732 doi:10.3389/fchem.2019.00509 (2019).

733 24 Janizek, J. D., Celik, S. & Lee, S.-I., doi:10.1101/331769 (2018).

734 25 He, L. *et al.* Patient-Customized Drug Combination Prediction and Testing for T-cell
735 Prolymphocytic Leukemia Patients. *Cancer Res* **78**, 2407-2418,
736 doi:10.1158/0008-5472.CAN-17-3644 (2018).

737 26 lanevski, A. *et al.* Prediction of drug combination effects with a minimal set of
738 experiments. *Nat Mach Intell* **1**, 568-577, doi:10.1038/s42256-019-0122-4 (2019).

739 27 Wu, L. *et al.* Machine learning methods, databases and tools for drug combination
740 prediction. *Briefings in Bioinformatics* (2021).

741 28 Preuer, K. *et al.* DeepSynergy: predicting anti-cancer drug synergy with Deep Learning.
742 *Bioinformatics* **Vol.34**, 1538-1546, doi:10.1093/bioinformatics/btx806 (2018).

743 29 Kuru, H. I., Tastan, O. & Cicek, E. MatchMaker: A Deep Learning Framework for Drug
744 Synergy Prediction. *IEEE/ACM Transactions on Computational Biology and*
745 *Bioinformatics*, 1-1, doi:10.1109/tcbb.2021.3086702 (2021).

746 30 Chen, G., Tsoi, A., Xu, H. & Zheng, W. J. Predict effective drug combination by deep belief
747 network and ontology fingerprints. *J Biomed Inform* **85**, 149-154,
748 doi:10.1016/j.jbi.2018.07.024 (2018).

749 31 Jiang, P. *et al.* Deep graph embedding for prioritizing synergistic anticancer drug
750 combinations. *Comput Struct Biotechnol J* **18**, 427-438, doi:10.1016/j.csbj.2020.02.006
751 (2020).

752 32 Jiang, P. *et al.* Deep graph embedding for prioritizing synergistic anticancer drug
753 combinations. *Computational and structural biotechnology journal* **18**, 427-438 (2020).

754 33 brahim Kuru, H., Tastan, O. & Cicek, E. Matchmaker: A deep learning framework for drug
755 synergy prediction. *IEEE/ACM Transactions on Computational Biology and Bioinformatics*
756 (2021).

757 34 KalantarMotamedi, Y., Eastman, R. T., Guha, R. & Bender, A. A systematic and
758 prospectively validated approach for identifying synergistic drug combinations against
759 malaria. *Malaria journal* **17**, 1-15 (2018).

760 35 Gayvert, K. M. *et al.* A computational approach for identifying synergistic drug
761 combinations. *PLoS computational biology* **13**, e1005308 (2017).

762 36 Li, X. *et al.* Prediction of synergistic anti-cancer drug combinations based on drug target
763 network and drug induced gene expression profiles. *Artificial intelligence in medicine* **83**,
764 35-43 (2017).

765 37 Lo, A. W., Siah, K. W. & Wong, C. H. Machine learning with statistical imputation for
766 predicting drug approvals. *Available at SSRN 2973611* (2018).

767 38 Sidorov, P., Naulaerts, S., Ariey-Bonnet, J., Pasquier, E. & Ballester, P. J. Predicting
768 synergism of cancer drug combinations using NCI-ALMANAC data. *Frontiers in*
769 *chemistry* **7**, 509 (2019).

770 39 Sun, Y., Xiong, Y., Xu, Q. & Wei, D. A hadoop-based method to predict potential effective

771 drug combination. *BioMed research international* **2014** (2014).

772 40 Zhu, J. *et al.* Prediction of drug efficacy from transcriptional profiles with deep learning.
773 *Nature Biotechnology*, 1-9 (2021).

774 41 Preuer, K. *et al.* DeepSynergy: predicting anti-cancer drug synergy with Deep Learning.
775 *Bioinformatics* **34**, 1538-1546 (2018).

776 42 Giaccone, G. *et al.* Cisplatin and etoposide combination chemotherapy for locally
777 advanced or metastatic thymoma. A phase II study of the European Organization for
778 Research and Treatment of Cancer Lung Cancer Cooperative Group. *Journal of clinical
779 oncology* **14**, 814-820 (1996).

780 43 Humans, I. W. G. o. t. E. o. C. R. t. in *Pharmaceuticals* (International Agency for
781 Research on Cancer, 2012).

782 44 Kier, M. G. *et al.* Prognostic factors and treatment results after bleomycin, etoposide, and
783 cisplatin in germ cell cancer: a population-based study. *European urology* **71**, 290-298
784 (2017).

785 45 Akazawa, R. *et al.* Temozolomide and etoposide combination for the treatment of
786 relapsed osteosarcoma. *Japanese Journal of Clinical Oncology* **50**, 948-952 (2020).

787 46 Carrillo, J. A., Hsu, F. P., Delashaw, J. & Bota, D. Efficacy and safety of bevacizumab and
788 etoposide combination in patients with recurrent malignant gliomas who have failed
789 bevacizumab. *Reviews in Health Care* **5**, 23-32 (2014).

790 47 Westhus, J. *et al.* Etoposide Combined with FLAG Salvage Therapy Is Effective in Multiple
791 Relapsed/Refractory Acute Myeloid leukemia. *Acta haematologica* **143**, 438-445 (2020).

792 48 Lian, B. *et al.* Clinical Benefit of Sorafenib Combined with Paclitaxel and Carboplatin to a
793 Patient with Metastatic Chemotherapy-Refractory Testicular Tumors. *The oncologist* **24**,
794 e1437 (2019).

795 49 Choi, K. H. *et al.* Synergistic activity of paclitaxel, sorafenib, and radiation therapy in
796 advanced renal cell carcinoma and breast cancer. *Translational oncology* **12**, 381-388
797 (2019).

798 50 Nawara, H. M. *et al.* Paclitaxel and sorafenib: The effective combination of suppressing
799 the self-renewal of cancer stem cells. *Cancers* **12**, 1360 (2020).

800 51 Berruti, A. *et al.* Phase II study of weekly paclitaxel and sorafenib as second/third-line
801 therapy in patients with adrenocortical carcinoma. *European journal of endocrinology*
802 **166**, 451 (2012).

803 52 Janku, F. *et al.* Dose-escalation study of vemurafenib with sorafenib or crizotinib in
804 patients with BRAF-mutated advanced cancers. *Cancer* **127**, 391-402 (2021).

805 53 Cheng, F., Kovács, I. A. & Barabási, A.-L. Network-based prediction of drug combinations.
806 *Nature communications* **10**, 1-11 (2019).

807 54 Zhou, Y. *et al.* Network-based drug repurposing for novel coronavirus
808 2019-nCoV/SARS-CoV-2. *Cell discovery* **6**, 1-18 (2020).

809 55 Yang, J., Xu, Z., Wu, W., Chu, Q. & Zhang, Q. GraphSynergy: Network Inspired Deep
810 Learning Model for Anti-Cancer Drug Combination Prediction. (2021).

811 56 Cheng, F. *et al.* A genome-wide positioning systems network algorithm for in silico drug
812 repurposing. *Nature communications* **10**, 1-14 (2019).

813 57 Kim, D.-S., Camacho, C. V. & Kraus, W. L. Alternate therapeutic pathways for PARP
814 inhibitors and potential mechanisms of resistance. *Experimental & molecular medicine*

815 **53**, 42-51 (2021).

816 58 Li, H. *et al.* PARP inhibitor resistance: the underlying mechanisms and clinical implications.
817 *Molecular cancer* **19**, 1-16 (2020).

818 59 Truong, S. *et al.* (AACR, 2021).

819 60 Jasek, E., Gajda, M., Lis, G. J., Jasińska, M. & Litwin, J. A. Combinatorial effects of PARP
820 inhibitor PJ34 and histone deacetylase inhibitor vorinostat on leukemia cell lines.
821 *Anticancer Research* **34**, 1849-1856 (2014).

822 61 Rasmussen, R. D., Gajjar, M. K., Jensen, K. E. & Hamerlik, P. Enhanced efficacy of
823 combined HDAC and PARP targeting in glioblastoma. *Molecular oncology* **10**, 751-763
824 (2016).

825 62 Chao, O. S. & Goodman, O. B. Synergistic loss of prostate cancer cell viability by
826 coinhibition of HDAC and PARP. *Molecular cancer research* **12**, 1755-1766 (2014).

827 63 Kruglov, O., Wu, X., Hwang, S. T. & Akilov, O. E. The synergistic proapoptotic effect of
828 PARP-1 and HDAC inhibition in cutaneous T-cell lymphoma is mediated via Blimp-1.
829 *Blood advances* **4**, 4788-4797 (2020).

830 64 Baldan, F. *et al.* Synergy between HDAC and PARP inhibitors on proliferation of a human
831 anaplastic thyroid cancer-derived cell line. *International journal of endocrinology* **2015**
832 (2015).

833 65 Valdez, B. C. *et al.* Combination of a hypomethylating agent and inhibitors of PARP and
834 HDAC traps PARP1 and DNMT1 to chromatin, acetylates DNA repair proteins,
835 down-regulates NuRD and induces apoptosis in human leukemia and lymphoma cells.
836 *Oncotarget* **9**, 3908 (2018).

837 66 Yu, X. *et al.* Modulation of p53, ErbB1, ErbB2, and Raf-1 expression in lung cancer cells by
838 depsipeptide FR901228. *Journal of the National Cancer Institute* **94**, 504-513 (2002).

839 67 Momeny, M. *et al.* Blockade of nuclear factor- κ B (NF- κ B) pathway inhibits growth and
840 induces apoptosis in chemoresistant ovarian carcinoma cells. *The international journal of*
841 *biochemistry & cell biology* **99**, 1-9 (2018).

842 68 Wang, J., Kho, D., Zhou, J.-Y., Davis, R. J. & Wu, G. S. MKP-1 suppresses PARP-1
843 degradation to mediate cisplatin resistance. *Oncogene* **36**, 5939-5947 (2017).

844 69 Chou, T.-C. Theoretical basis, experimental design, and computerized simulation of
845 synergism and antagonism in drug combination studies. *Pharmacological reviews* **58**,
846 621-681 (2006).

847 70 García-Valdivia, A. A. *et al.* Anti-cancer and anti-inflammatory activities of a new family
848 of coordination compounds based on divalent transition metal ions and
849 indazole-3-carboxylic acid. *Journal of Inorganic Biochemistry* **215**, 111308 (2021).

850 71 Marcar, L. *et al.* Acquired resistance of EGFR-mutated lung cancer to tyrosine kinase
851 inhibitor treatment promotes PARP inhibitor sensitivity. *Cell reports* **27**, 3422-3432.
852 e3424 (2019).

853 72 Moore, K. N. *et al.* Niraparib monotherapy for late-line treatment of ovarian cancer
854 (QUADRA): a multicentre, open-label, single-arm, phase 2 trial. *The Lancet Oncology* **20**,
855 636-648 (2019).

856 73 Patil, P. P., Sanklecha, V. M., Aher, S. J. & Sitaram, M. D. Topoisomerase an Ideal Target
857 for Treatment of Cancer.

858 74 Hande, K. R. Topoisomerase II inhibitors. *Update on cancer therapeutics* **3**, 13-26 (2008).

859 75 Berndsen, R. H., Swier, N., van Beijnum, J. R. & Nowak-Sliwinska, P. Colorectal cancer
860 growth retardation through induction of apoptosis, using an optimized synergistic
861 cocktail of axitinib, erlotinib, and dasatinib. *Cancers* **11**, 1878 (2019).

862 76 Wiegmans, A. P., Yap, P.-Y., Ward, A., Lim, Y. C. & Khanna, K. K. Differences in expression
863 of key DNA damage repair genes after epigenetic-induced BRCAness dictate synthetic
864 lethality with PARP1 inhibition. *Molecular cancer therapeutics* **14**, 2321-2331 (2015).

865 77 Mizutani, H. *et al.* Romidepsin (FK228), a potent histone deacetylase inhibitor, induces
866 apoptosis through the generation of hydrogen peroxide. *Cancer science* **101**, 2214-2219
867 (2010).

868 78 Shi, Y. *et al.* Romidepsin (FK228) regulates the expression of the immune checkpoint
869 ligand PD-L1 and suppresses cellular immune functions in colon cancer. *Cancer*
870 *Immunology, Immunotherapy* **70**, 61-73 (2021).

871 79 Kim, J. H. *et al.* Dexamethasone inhibits hypoxia-induced epithelial-mesenchymal
872 transition in colon cancer. *World Journal of Gastroenterology: WJG* **21**, 9887 (2015).

873 80 Deng, J. *et al.* Everolimus and plicamycin specifically target chemoresistant colorectal
874 cancer cells of the CMS4 subtype. *Cell death & disease* **12**, 1-11 (2021).

875 81 Zhao, Y. *et al.* Inhibition of the transcription factor Sp1 suppresses colon cancer stem cell
876 growth and induces apoptosis in vitro and in nude mouse xenografts. *Oncology reports*
877 **30**, 1782-1792 (2013).

878 82 Seligmann, J. F. *et al.* Inhibition of WEE1 is effective in TP53-and RAS-mutant metastatic
879 colorectal cancer: a randomized trial (FOCUS4-C) comparing adavosertib (AZD1775)
880 with active monitoring. *Journal of Clinical Oncology* (2021).

881 83 Watanabe, N., Broome, M. & Hunter, T. Regulation of the human WEE1Hu CDK tyrosine
882 15-kinase during the cell cycle. *The EMBO journal* **14**, 1878-1891 (1995).

883 84 Akinleye, A., Furqan, M., Mukhi, N., Ravella, P. & Liu, D. MEK and the inhibitors: from
884 bench to bedside. *Journal of hematology & oncology* **6**, 1-11 (2013).

885 85 Lawal, B. *et al.* A preclinical report of a cobimetinib-inspired novel anticancer
886 small-molecule scaffold of isoflavones, NSC777213, for targeting PI3K/AKT/mTOR/MEK
887 in multiple cancers. *American Journal of Cancer Research* **11**, 2590 (2021).

888 86 Jalal, T. K. Cytotoxic effects and mechanisms of cell death of *Artocarpus altilis* on human
889 breast, colon, lung and skin cancer cells. (2018).

890 87 Dragoi, A. & Alexandru, O. PLANT-DERIVED CHEMOTHERAPEUTICS DRUGS FOR
891 CANCER CHEMOTHERAPY. *Medico Oncology* **1**, 28-37 (2020).

892 88 Capasso, A. Vinorelbine in cancer therapy. *Current drug targets* **13**, 1065-1071 (2012).

893 89 Provencio, M., Isla, D., Sánchez, A. & Cantos, B. Inoperable stage III non-small cell lung
894 cancer: Current treatment and role of vinorelbine. *Journal of thoracic disease* **3**, 197
895 (2011).

896 90 Liu, X., Yue, P., Zhou, Z., Khuri, F. R. & Sun, S.-Y. Death receptor regulation and
897 celecoxib-induced apoptosis in human lung cancer cells. *Journal of the National Cancer*
898 *Institute* **96**, 1769-1780 (2004).

899 91 Zhou, S., Zhou, C., Xu, J. & Lv, M. P2-327: First-line chemotherapy of vinorelbine/cisplatin
900 (NP) combined with cyclooxygenase-2 inhibitor celecoxib in advanced non-small-cell
901 lung cancer (NSCLC). *Journal of Thoracic Oncology* **2**, S702-S703 (2007).

902 92 Ettinger, D. in *Seminars in oncology*. 31-38.

903 93 Masters, G. A. *et al.* Phase I study of vinorelbine and ifosfamide in advanced
904 non-small-cell lung cancer. *Journal of clinical oncology* **15**, 884-892 (1997).

905 94 Baldini, E. *et al.* Phase II study of vinorelbine/ifosfamide/cisplatin for the treatment of
906 advanced non-small-cell lung cancer. *Annals of oncology* **7**, 747-749 (1996).

907 95 Chen, M.-C., Hsu, S.-L., Lin, H. & Yang, T.-Y. Retinoic acid and cancer treatment.
908 *Biomedicine* **4**, 1-6 (2014).

909 96 Alizadeh, F. *et al.* Retinoids and their biological effects against cancer. *International*
910 *immunopharmacology* **18**, 43-49 (2014).

911 97 Liang, Z., Li, J. & Zhu, B. Lung cancer combination treatment: evaluation of the synergistic
912 effect of cisplatin prodrug, vinorelbine and retinoic acid when co-encapsulated in a
913 multi-layered nano-platform. *Drug Design, Development and Therapy* **14**, 4519 (2020).

914 98 Zhu, Y.-H. *et al.* Synergistic effect of retinoic acid polymeric micelles and prodrug for the
915 pharmacodynamic evaluation of tumor suppression. *Frontiers in pharmacology* **10**, 447
916 (2019).

917 99 Smith, P. J., Morgan, S. A., Fox, M. E. & Watson, J. V. Mitoxantrone-DNA binding and the
918 induction of topoisomerase II associated DNA damage in multi-drug resistant small cell
919 lung cancer cells. *Biochemical pharmacology* **40**, 2069-2078 (1990).

920 100 Zagidullin, B. *et al.* DrugComb: an integrative cancer drug combination data portal.
921 *Nucleic acids research* **47**, W43-W51 (2019).

922 101 O'Neil, J. *et al.* An unbiased oncology compound screen to identify novel combination
923 strategies. *Molecular cancer therapeutics* **15**, 1155-1162 (2016).

924 102 Holbeck, S. L. *et al.* The National Cancer Institute ALMANAC: a comprehensive screening
925 resource for the detection of anticancer drug pairs with enhanced therapeutic activity.
926 *Cancer research* **77**, 3564-3576 (2017).

927 103 Forcina, G. C., Conlon, M., Wells, A., Cao, J. Y. & Dixon, S. J. Systematic quantification of
928 population cell death kinetics in mammalian cells. *Cell systems* **4**, 600-610. e606 (2017).

929 104 Licciardello, M. P. *et al.* A combinatorial screen of the CLOUD uncovers a synergy
930 targeting the androgen receptor. *Nature chemical biology* **13**, 771-778 (2017).

931 105 Bliss, C. I. The toxicity of poisons applied jointly 1. *Annals of applied biology* **26**, 585-615
932 (1939).

933 106 Borisy, A. A. *et al.* Systematic discovery of multicomponent therapeutics. *Proceedings of*
934 *the National Academy of Sciences* **100**, 7977-7982 (2003).

935 107 Loewe, S. The problem of synergism and antagonism of combined drugs.
936 *Arzneimittelforschung* **3**, 285-290 (1953).

937 108 Yadav, B., Wennerberg, K., Aittokallio, T. & Tang, J. Searching for drug synergy in
938 complex dose-response landscapes using an interaction potency model. *Computational*
939 *and structural biotechnology journal* **13**, 504-513 (2015).

940 109 Malyutina, A. *et al.* Drug combination sensitivity scoring facilitates the discovery of
941 synergistic and efficacious drug combinations in cancer. *PLoS computational biology* **15**,
942 e1006752 (2019).

943 110 Wishart, D. S. *et al.* DrugBank 5.0: a major update to the DrugBank database for 2018.
944 *Nucleic acids research* **46**, D1074-D1082 (2018).

945 111 Menche, J. *et al.* Uncovering disease-disease relationships through the incomplete
946 interactome. *Science* **347** (2015).

947 112 Wang, Y. *et al.* PubChem: a public information system for analyzing bioactivities of small
948 molecules. *Nucleic acids research* **37**, W623-W633 (2009).

949 113 Cao, Y., Charisi, A., Cheng, L.-C., Jiang, T. & Girke, T. ChemmineR: a compound mining
950 framework for R. *Bioinformatics* **24**, 1733-1734 (2008).

951 114 Camp, D., Garavelas, A. & Campitelli, M. Analysis of physicochemical properties for drugs
952 of natural origin. *Journal of natural products* **78**, 1370-1382 (2015).

953 115 Raevsky, O. A. Physicochemical descriptors in property-based drug design. *Mini reviews
954 in medicinal chemistry* **4**, 1041-1052 (2004).

955 116 Gleeson, M. P., Leeson, P. D. & van de Waterbeemd, H. in *The Handbook of Medicinal
956 Chemistry* 1-31 (2014).

957 117 O'Boyle, N. M., Morley, C. & Hutchison, G. R. Pybel: a Python wrapper for the OpenBabel
958 cheminformatics toolkit. *Chemistry Central Journal* **2**, 1-7 (2008).

959 118 Wegner, J. Joelib/joelib2. *Germany: Department of Computer Science, University of
960 Tübingen* (2005).

961 119 Zhang, P. *et al.* A protein network descriptor server and its use in studying protein,
962 disease, metabolic and drug targeted networks. *Briefings in bioinformatics* **18**,
963 1057-1070 (2017).

964 120 Consortium, U. UniProt: a hub for protein information. *Nucleic acids research* **43**,
965 D204-D212 (2015).

966 121 Zhang, P. *et al.* PROFEAT update: a protein features web server with added facility to
967 compute network descriptors for studying omics-derived networks. *Journal of molecular
968 biology* **429**, 416-425 (2017).

969 122 Rao, H., Zhu, F., Yang, G., Li, Z. & Chen, Y. Z. Update of PROFEAT: a web server for
970 computing structural and physicochemical features of proteins and peptides from amino
971 acid sequence. *Nucleic acids research* **39**, W385-W390 (2011).

972 123 Li, Z.-R. *et al.* PROFEAT: a web server for computing structural and physicochemical
973 features of proteins and peptides from amino acid sequence. *Nucleic acids research* **34**,
974 W32-W37 (2006).

975 124 Chen, T. & Guestrin, C. in *Proceedings of the 22nd acm sigkdd international conference
976 on knowledge discovery and data mining*. 785-794.

977 125 Pedregosa, F. *et al.* Scikit-learn: Machine learning in Python. *the Journal of machine
978 Learning research* **12**, 2825-2830 (2011).

979 126 Pedregosa, F. *et al.* Scikit-learn: Machine Learning in Python. *J Mach Learn Res* **12**,
980 2825-2830 (2011).

981 127 Chen, T. Q. & Guestrin, C. XGBoost: A Scalable Tree Boosting System. *Kdd'16:
982 Proceedings of the 22nd Acm Sigkdd International Conference on Knowledge Discovery
983 and Data Mining*, 785-794, doi:10.1145/2939672.2939785 (2016).

984 128 Kuru, H. I., Tastan, O. & Cicek, A. E. MatchMaker: A Deep Learning Framework for Drug
985 Synergy Prediction. (2020).

986 129 Cao, Z. czwlines/DT-GRN v.1.0.0 (accessed 15 February 2022). doi: [http://doi.org/
987 10.5281/zenodo.6088766](http://doi.org/10.5281/zenodo.6088766).

988

989 **Acknowledgements**

990 This work is supported by National Natural Science Foundation of China (62103436), Natural
991 Science Foundation of Fujian Province of China (No. 2020J06001), and Youth Innovation Fund of
992 Xiamen (No. 3502ZZ20206059).

993 **Author contributions**

994 X.B., S.H., J.S., Y.W., Z.C. conceived the idea, designed the study and wrote the manuscript. Y.W.,
995 Z.C., L.W., C.D. conducted the investigation. Y.W., L.W., J.W., D.L. acquired data. Z.C., Y.W.
996 designed and implemented the proposed method. Y.W., Z.C., Z.W. analyzed the results. Y.W., Z.C.,
997 performed visualizations. Y.Z. performed the in vitro experiments. X.B., S.H., J.S. supervised the
998 research.

999 **Competing interests**

1000 The authors declare no competing interests.

1001

1002

1003

Supplementary Files

This is a list of supplementary files associated with this preprint. Click to download.

- [Supplementaryinformation.pdf](#)